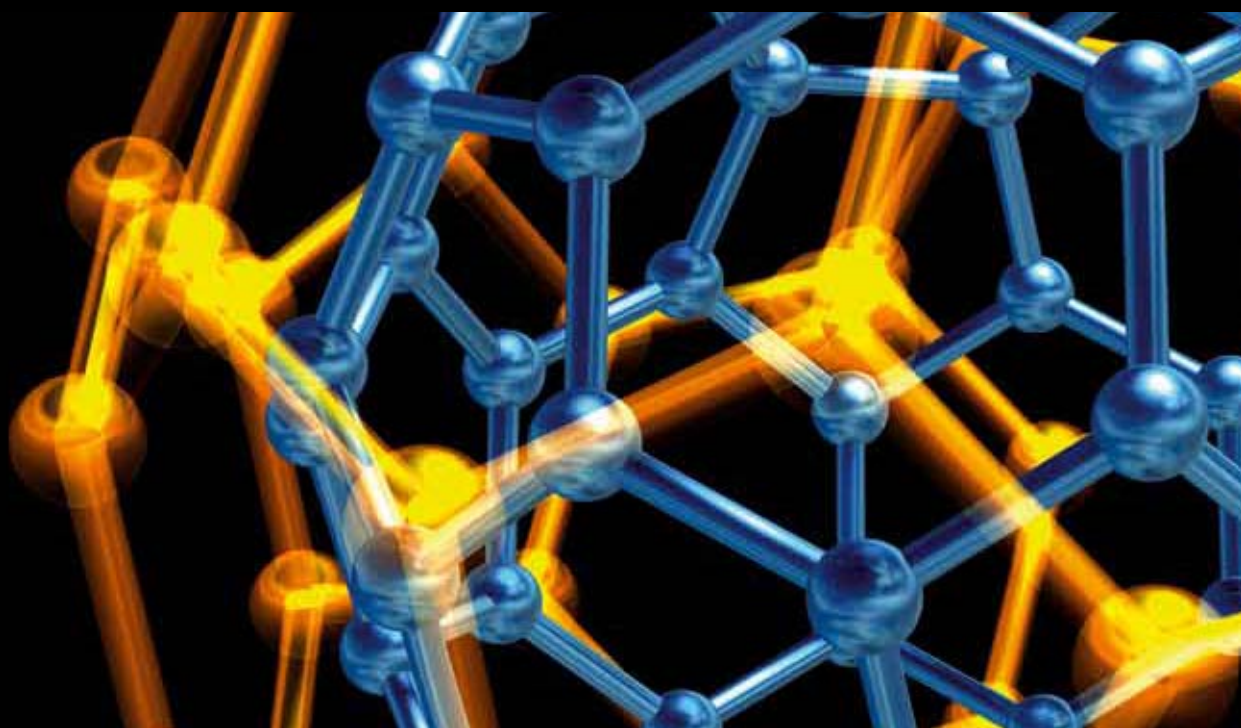


# FUNCTIONAL NANOMATERIALS

GUEST EDITORS: HABIB M. PATHAN, RAJARAM S. MANE, YAHYA A. ISMAIL,  
ANQIAH SUBRAMANIA, WEGDAN RAMADAN, AND SHARAD D. BHAGAT





---

# **Functional Nanomaterials**

Journal of Nanotechnology

---

## **Functional Nanomaterials**

Guest Editors: Habib M. Pathan, Rajaram S. Mane,  
Yahya A. Ismail, Angaiah Subramania, Wegdan Ramadan,  
and Sharad D. Bhagat



---

Copyright © 2012 Hindawi Publishing Corporation. All rights reserved.

This is a special issue published in "Journal of Nanotechnology." All articles are open access articles distributed under the Creative Commons Attribution License, which permits unrestricted use, distribution, and reproduction in any medium, provided the original work is properly cited.

## Editorial Board

Simon Joseph Antony, UK  
Y. Bando, Japan  
B. Bhushan, USA  
Felix A. Buot, USA  
Carlos R. Cabrera, Puerto Rico  
John A. Capobianco, Canada  
Franco Cerrina, USA  
Gan Moog Chow, Singapore  
Jeffery L. Coffey, USA  
Dmitriy A. Dikin, USA  
Dimitris Drikakis, UK  
H. D. Espinosa, USA  
John S. Foord, UK  
E. Goldys, Australia  
Lambertus Hesselink, USA  
Joseph Irudayaraj, USA

Niraj K. Jha, USA  
Miguel Jose-Yacamán, USA  
Valery Khabashesku, USA  
Yoke Khin Yap, USA  
Sakhrat Khizroev, USA  
Andrei Kolmakov, USA  
Charles M. Lieber, USA  
Charles M. Lukehart, USA  
A. H. Makhlof, Germany  
Constantinos Mavroidis, USA  
Vincent Meunier, USA  
Paolo Milani, Italy  
Oded Millo, Israel  
M. Grant Norton, USA  
R. Lee Penn, USA  
S. N. Piramanayagam, Singapore

A. M. Rao, USA  
Paresh Chandra Ray, USA  
Benjaram M. Reddy, India  
Federico Rosei, Canada  
Mehmet Sarikaya, USA  
Jorge M. Seminario, USA  
V. Shalaev, USA  
Mahi R. Singh, Canada  
Bobby G. Sumpster, USA  
Xiao Wei Sun, Singapore  
Weihong Tan, USA  
O. K. Tan, Singapore  
Thomas Thundat, USA  
Boris I. Yakobson, USA  
Nan Yao, USA  
Chuan Jian Zhong, USA

## Contents

**Functional Nanomaterials**, Habib M. Pathan, Rajaram S. Mane, Yahya A. Ismail, Angaiah Subramania, Wegdan Ramadan, and Sharad D. Bhagat  
Volume 2012, Article ID 732368, 2 pages

**Characterization of Titanium Oxide Nanoparticles Obtained by Hydrolysis Reaction of Ethylene Glycol Solution of Alkoxide**, Naofumi Uekawa, Naoya Endo, Keisuke Ishii, Takashi Kojima, and Kazuyuki Kakegawa  
Volume 2012, Article ID 102361, 8 pages

**Direct Vapor-Phase Bromination of Multiwall Carbon Nanotubes**, Ilya Mazov, Dmitry Krasnikov, Andrey Stadnichenko, Vladimir Kuznetsov, Anatoly Romanenko, Olga Anikeeva, and Evgeniy Tkachev  
Volume 2012, Article ID 954084, 5 pages

**Synthesis of 1D, 2D, and 3D ZnO Polycrystalline Nanostructures Using the Sol-Gel Method**, Yung-Kuan Tseng, Ming-Hung Chuang, Yen-Cheng Chen, and Chao-Hsien Wu  
Volume 2012, Article ID 712850, 8 pages

**Interconnected TiO<sub>2</sub> Nanowire Networks for PbS Quantum Dot Solar Cell Applications**, Fan Xu, Jaime Benavides, Xin Ma, and Sylvain G. Cloutier  
Volume 2012, Article ID 709031, 6 pages

**Electrical Transport Properties of Multilayered Single-Walled Carbon Nanotube Films**, Yanli Zhao and Wenzhi Li  
Volume 2012, Article ID 601582, 5 pages

## Editorial

# Functional Nanomaterials

**Habib M. Pathan,<sup>1</sup> Rajaram S. Mane,<sup>2</sup> Yahya A. Ismail,<sup>3</sup> Angaiah Subramania,<sup>4</sup>  
Wegdan Ramadan,<sup>5</sup> and Sharad D. Bhagat<sup>6</sup>**

<sup>1</sup>Advanced Physics Laboratory, Department of Physics, University of Pune, Pune 411007, India

<sup>2</sup>Center for Nanomaterials and Energy Devices, School of Physical Sciences, Swami Ramanand Teerth Marathwada University, Nanded 431606, India

<sup>3</sup>Department of Biological Sciences and Chemistry, University of Nizwa, Nizwa 616, Oman

<sup>4</sup>Centre for Nanoscience and Technology, Pondicherry University, Puducherry 605014, India

<sup>5</sup>Department of Physics, Alexandria University, Alexandria, Egypt

<sup>6</sup>Department of Chemistry and Biochemistry, Florida State University, Tallahassee, FL 32306, USA

Correspondence should be addressed to Habib M. Pathan, pathan@physics.unipune.ac.in

Received 6 May 2012; Accepted 6 May 2012

Copyright © 2012 Habib M. Pathan et al. This is an open access article distributed under the Creative Commons Attribution License, which permits unrestricted use, distribution, and reproduction in any medium, provided the original work is properly cited.

The impetus of scientific community around the world lately has been on nanoscience and technology as the researchers have envisioned great many applications for these materials earning them rightly the name “functional nanomaterials.” This domain of materials is special since they display extraordinary transitions in their properties in their size regime as compared to their bulk counterparts. The electrical, electronic, optical, thermal, mechanical, or magnetic properties of these classes of materials have opened great avenues for many important applications and redefined and improved the efficiencies of the devices generated out of them.

The novel era of functional nanomaterials has goaded change in the face as well as phase of all the materials and facilitated design of materials customized to the needs of the mankind by manipulating matter at the nanoscopic level.

The world is and will keep on witnessing the demand for new nanomaterials for multifarious high-tech and industrial applications. This special issue is aimed at bringing out an overview of the latest advances in the field of nanomaterials with special emphasis on synthesis and applications highlighting greater strides in the field. Nanoscience and technology being an interdisciplinary field encompasses a wide range of subjects like physics, chemistry, biology, biotechnology, engineering, mathematics, and so forth. In view of this the present issue broadly covers carbon-based, nanomaterials, their synthesis and applications, wide

bandgap semiconductors, and their applications as nanomaterials in sensing, photocatalysis and photovoltaics.

The present issue covers syntheses of titania reported by Cloutier and coworkers and Uekawa et al. of which the former deals with facile preparation of porous titania nanostructures and their role in the enhanced power conversion in heterojunction solar cells. The latter presents a large surface area TiO<sub>2</sub> nanoparticles' synthesis through hydrolysis. Another wide bandgap semiconductor, the richest family of nanostructures among all materials, the much talked about ZnO, is also accommodated. Tseng et al. employed various polyol solvents to synthesize zinc oxide polycrystalline nanostructures in the form of fibers (1D), rhombic flakes (2D), and spheres (3D). Thus formed ZnO structures were applied in the degradation of methylene blue to compare their photocatalytic efficiency.

Keeping in view the promising applications of carbon nanotubes (CNTs), two papers are included on CNTs. Zhao and Li reported an improved layer-by-layer vacuum filtration method for the fabrication of single-walled carbon nanotube (SWCNT) films aiming at a series of SWCNT films with controllable thickness and density. The electrical transport properties of the multi-layered SWCNT films have been investigated. Mazov et al. present the simple procedure of the vapor-phase bromination of multiwall carbon nanotubes (MWNTs) at moderate temperatures. MWNTs with average

diameter  $9 \pm 3$  nm were treated with bromine vapours to produce Br-functionalized products.

*Habib M. Pathan*  
*Rajaram S. Mane*  
*Yahya A. Ismail*  
*Angaiah Subramania*  
*Wegdan Ramadan*  
*Sharad D. Bhagat*

## Research Article

# Characterization of Titanium Oxide Nanoparticles Obtained by Hydrolysis Reaction of Ethylene Glycol Solution of Alkoxide

Naofumi Uekawa, Naoya Endo, Keisuke Ishii, Takashi Kojima, and Kazuyuki Kakegawa

Graduate School of Engineering, Chiba University, 1-33 Yayoi-cho, Inage-ku, Chiba-shi 263-8522, Japan

Correspondence should be addressed to Naofumi Uekawa, uekawa@faculty.chiba-u.jp

Received 1 December 2011; Revised 15 February 2012; Accepted 29 February 2012

Academic Editor: Wegdan Ramadan

Copyright © 2012 Naofumi Uekawa et al. This is an open access article distributed under the Creative Commons Attribution License, which permits unrestricted use, distribution, and reproduction in any medium, provided the original work is properly cited.

Transparent and stable sols of titanium oxide nanoparticles were obtained by heating a mixture of ethylene glycol solution of titanium tetraisopropoxide (TIP) and a  $\text{NH}_3$  aqueous solution at 368 K for 24 h. The concentration of  $\text{NH}_3$  aqueous solution affected the structure of the obtained titanium oxide nanoparticles. For  $\text{NH}_3$  aqueous solution concentrations higher than 0.2 mol/L, a mixture of anatase  $\text{TiO}_2$  nanoparticles and layered titanate nanoparticles was obtained. The obtained sol was very stable without formation of aggregated precipitates and gels. Coordination of ethylene glycol to  $\text{Ti}^{4+}$  ions inhibited the rapid hydrolysis reaction and aggregation of the obtained nanoparticles. The obtained titanium oxide nanoparticles had a large specific surface area: larger than 350  $\text{m}^2/\text{g}$ . The obtained titanium oxide nanoparticles showed an enhanced adsorption towards the cationic dye molecules. The selective adsorption corresponded to presence of layered titanate on the obtained anatase  $\text{TiO}_2$  nanoparticles.

## 1. Introduction

Titanium dioxide ( $\text{TiO}_2$  titania) is an n-type oxide semiconductor that shows photocatalytic activity and photoconductivity [1, 2]. Several various applications of  $\text{TiO}_2$  particles have been studied in recent years, as photocatalysts and to solar cells, UV-shielding materials and electric devices [3–6]. For these applications, development of a simple synthesis method to obtain  $\text{TiO}_2$  nanoparticles with highly homogeneous dispersion has been required [7, 8].  $\text{TiO}_2$  nanoparticles are also useful in many important applications for improving environmental problems [9, 10]. These nanoparticles can be used for formation of  $\text{TiO}_2$  thin films with optical transparency and photocatalyst activity. Furthermore, surface characteristics of  $\text{TiO}_2$  nanoparticles strongly affect the application area of  $\text{TiO}_2$  nanoparticles. For example, Grätzel developed photoelectrochemical systems with dye-sensitized anatase  $\text{TiO}_2$  semiconductor electrodes [11, 12]. The characteristics of these solar cells depend on adsorption interaction between dye molecules and  $\text{TiO}_2$  nanoparticle surface. Therefore, it is also important to control molecular adsorption properties of  $\text{TiO}_2$  nanoparticles.

Rath et al. prepared size-controlled  $\text{TiO}_2$  nanoparticles in reverse micelles using a surfactant Aerosol-OT (AOT) [13]. Zaki et al. obtained anatase  $\text{TiO}_2$  nanoparticles through hydrolysis of ethanol solution of titanium tetraisopropoxide by adding nitric acid [14]. They examined an adsorption of amine molecules to investigate the surface adsorption sites. Nakayama and Hyashi prepared stable sols of  $\text{TiO}_2$  with surface modification of carboxylic acid and amine [15]. Some reports have also described methods for preparation of  $\text{TiO}_2$  nanoparticles and stable sols using peroxotitanic acid as a precursor [16].

This study describes examination of a novel preparation method of titanium oxide nanoparticles and their stable sols through hydrolysis reaction of an ethylene glycol solution of titanium alkoxide with  $\text{NH}_3$  aqueous solution. Ethylene glycol easily coordinates to  $\text{Ti}^{4+}$  ions and controls the hydrolysis reaction [17, 18]. Furthermore,  $\text{NH}_3$  molecules also strongly coordinate to the  $\text{Ti}^{4+}$  ions. It is expected that restricting rapid hydrolysis reaction enables the production of titanium oxide nanoparticles without aggregation. Furthermore, surface characteristics of the titanium oxide nanoparticles were examined by measuring adsorption isotherms of cationic and anionic dye molecules.

## 2. Experiments

**2.1. Preparation of Titanium Oxide Nanoparticles and Their Sols.** The titanium oxide nanoparticles were prepared as follows. The 1 mol/L of  $\text{NH}_3$  aqueous solution was added to the 50 mL of ethylene glycol solution (0.1 mol/L) of titanium tetraisopropoxide (TIP). The total volume was adjusted to 100 mL. Under these circumstances no precipitate was observed, although an opaque solution was obtained. This solution was heated at 368 K for 24 h in a closed glass vessel, and a stable sol was obtained without precipitation. All chemicals used in this preparation were of reagent grade (Wako Pure Chemical Industries Ltd.). To control the particle size and surface properties of the obtained titanium oxide nanoparticles, the same synthetic process was also conducted using the  $\text{NH}_3$  (aq) with other concentrations. The concentrations were in the range of 0.1 mol/L–1 mol/L. Hereinafter, this concentration will be designated as  $[\text{NH}_3]$ .

To separate the obtained particles from the sol, 50 mL of the obtained sol was poured into a cellulose tube for dialysis, and the cellulose tube was soaked in 500 mL of  $\text{H}_2\text{O}$  for 3 h at room temperature. The 500 mL of  $\text{H}_2\text{O}$  was exchanged five times. Finally, the sol in the cellulose tube was dried at 348 K for 12 h.

Anatase  $\text{TiO}_2$  particles were also prepared using a simple hydrolysis reaction between Ti alkoxide and  $\text{H}_2\text{O}$ . The  $\text{H}_2\text{O}$  was added to 0.01 mol of TIP. Then the total volume was adjusted to 100 mL. The mixed solution of TIP and  $\text{H}_2\text{O}$  was kept in a closed glass beaker and heated at 368 K for 24 h. White precipitate was obtained using the hydrolysis reaction. The precipitate was separated by centrifugation at 3000 rpm for 5 min. The obtained precipitate was dried at 348 K for 24 h.

**2.2. Characterization.** The structure of the obtained particles was characterized using X-ray diffraction (XRD) (Cu  $K\alpha$  40 kV, 100 mA, MXP-18; Bruker AXS Co., Ltd.). The particle shape was observed using field emission scanning electron microscopy (FE-SEM; JSM-6330; JEOL) after osmium coating, which is one of the electroconductive film formation methods for electron microscope observation. It is the method for depositing osmium metal thin film on the sample surface by DC glow discharge in osmium oxide gas. The ultraviolet-visible (UV-VIS) spectra of the sols and the solutions were measured using quartz cell (UV2000; Hitachi Ltd.) with wavelengths of 300–800 nm, and the optical path length of the cell was 1 cm. Thermogravimetric analysis and differential thermal analysis (TG-DTA) were measured in the air with the flow rate = 100 mL/min. Weight of the used samples was 10 mg, and the rate of elevating temperature was 10 K/min. The upper limit of the measuring temperature was 1073 K. The  $\text{N}_2$  adsorption isotherms of the obtained powders were measured at 77 K by using the volumetric method (BELSORP-max, BEL Japan, Inc.) after pretreatment at 383 K in 1 mPa for 1 h. The used sample weight was ca. 0.1 g.

**2.3. Dye Adsorption Measurement.** Dye adsorption isotherms of the titanium oxide nanoparticles were measured as

described below. First, 50 mL of methylene blue aqueous solutions was prepared and adjusted to the following concentrations:  $1 \times 10^{-4}$  mol/L,  $2 \times 10^{-4}$  mol/L,  $3 \times 10^{-4}$  mol/L,  $4 \times 10^{-4}$  mol/L,  $6 \times 10^{-4}$  mol/L, and  $8 \times 10^{-4}$  mol/L. 0.05 g of the titanium oxide powder was added to 50 mL of each of the methylene blue aqueous solution. The pH values of the dye aqueous solution with dispersion of the titanium oxide powder were in the range from 6.5 to 7.5 before and after the adsorption. Each dye aqueous solution with the titanium oxide powder was stirred at 500 rpm at 298 K for 24 h to reach the equilibrium of dye adsorption. From each solution, 3 mL of the methylene blue aqueous solution was separated using filtration with a  $0.45 \mu\text{m}$  membrane filter. The optical absorbance of the corrected methylene blue aqueous solution at 655 nm was measured using a UV-VIS spectrometer (UV2000; Hitachi Ltd.). The methylene blue concentrations were calculated from the absorbance using a working curve. Measurements of the dye adsorption isotherm described above were also conducted using other dyes such as crystal violet, Evans blue, and eosin Y. The respective wavelengths used for estimating the dye aqueous solution concentrations of crystal violet, Evans blue, and eosin Y were 590 nm, 608 nm, and 517 nm.

## 3. Results and Discussion

**3.1. Characterization of the Obtained Titanium Oxide Nanoparticles.** Figure 1 portrays XRD patterns of the particles obtained by heating the mixture of ethylene glycol solution of TIP and  $\text{NH}_3$  (aq) at 368 K for 24 h. The XRD peaks in Figures 1(a)–1(e), as marked with open circles, can be assigned to anatase  $\text{TiO}_2$ . When the concentration of the  $\text{NH}_3$  (aq) concentration mixed with the ethylene glycol solution of TIP was 0.1 mol/L, the obtained titanium oxide was anatase  $\text{TiO}_2$  as shown in Figure 1(a). When the mixture of TIP and  $\text{H}_2\text{O}$  was heated at 368 K for 24 h, anatase  $\text{TiO}_2$  was also obtained as shown in Figure 1(e). In Figure 1(b), a very weak and broad peak around  $2\theta < 10^\circ$  can be assigned to layered titanate structure [19]. When the  $\text{NH}_3$  (aq) concentration became higher than 0.2 mol/L, the XRD peaks shown in Figures 1(b)–1(d) can be assigned to layered titanate acid lattice and anatase  $\text{TiO}_2$ . Accordingly, the  $\text{NH}_3$  (aq) concentration affected the crystal structure of the obtained particles. Furthermore, crystallite sizes were determined by using Scherrer's equation at the peak of anatase  $\text{TiO}_2$  (101) plane at  $2\theta = 25.8^\circ$ . The crystallite sizes determined from the XRD patterns of Figures 1(a)–1(e) were 4.68 nm, 4.60 nm, 2.88 nm, 2.27 nm, and 10.7 nm, respectively. Accordingly, a decrease in crystallite size was observed with increases in the  $\text{NH}_3$  (aq) concentration. Furthermore, the crystallite size of anatase  $\text{TiO}_2$  of Figure 1(a) was smaller than that of Figure 1(e). This result means that growth of the crystallite size of the anatase  $\text{TiO}_2$  particles was restricted by coordination of the coexisted  $\text{NH}_3$  and ethylene glycol molecules in the solution.

Figure 2 shows FE-SEM images of the obtained titanium oxide particles. Figures 2(a), 2(b), and 2(c), respectively, show FE-SEM images of particles obtained using the  $\text{NH}_3$

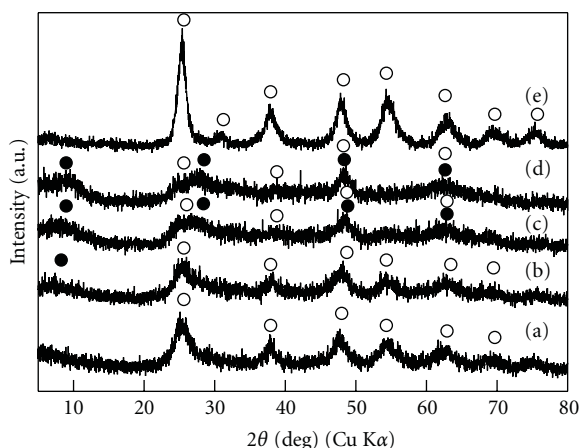


FIGURE 1: XRD patterns of the obtained particles by heating a mixture of ethylene glycol solution of TIP and  $\text{NH}_3$  (aq) at 368 K for 24 h. The  $\text{NH}_3$  (aq) concentrations were (a) 0.1 mol/L, (b) 0.2 mol/L, (c) 0.5 mol/L, (d) 1 mol/L, and (e) the particles obtained by heating the mixture of TIP and  $\text{H}_2\text{O}$  at 368 K for 24 h. ○: anatase  $\text{TiO}_2$  and ●: layered titanate.

(aq) at concentrations of 0.1 mol/L, 0.5 mol/L, and 1 mol/L. When the  $[\text{NH}_3]$  values were 0.1 mol/L, 0.5 mol/L, and 1 mol/L, the average particle sizes were 32.1 nm, 31.5 nm, and 28.0 nm, respectively. The particle sizes of the obtained titanium oxide particles were almost close to each other. The coordination of  $\text{NH}_3$  aqueous solution did not affect the particle size of the titanium oxide nanoparticles, although as discussed in Figure 1, the crystal structure was affected. The average particle sizes determined by FE-SEM images of the titanium oxide nanoparticles were larger than the crystallite sizes determined by using Scherrer's equation. This means that the particles observed in the FE-SEM images had aggregated structure of crystallites. Furthermore, when the  $\text{NH}_3$  (aq) concentration was more than 0.5 mol/L, the particle shape would change from spherical particles to plate particles. This will be one of the reasons of difference between the crystallite size and the average particle size.

To examine the residual organic molecules and the degree of the crystallization of the obtained nanoparticles, the TG-DTA curves were measured. Figure 3(a) shows the TG-DTA curve of the nanoparticles obtained by using the  $\text{NH}_3$  (aq) ( $[\text{NH}_3] = 0.1$  mol/L). The TG curve had 15.1% weight loss below 400 K. This weight loss corresponded to desorption of adsorbed  $\text{H}_2\text{O}$  on the nanoparticles. Furthermore, when the temperature was around 523 K, a steep decrease of weight was observed. According to the DTA curve, a sharp exothermic peak also appeared around 523 K. Therefore, the weight loss around 523 K corresponded to the oxidation of the TIP molecules which did not react in the hydrolysis reaction. The weight loss around this temperature was 8.1%. Furthermore, a slight decrease of weight (4.82%) occurred at temperatures of 530 K to 700 K. This weight loss corresponded to dehydration of surface OH groups and desorption of the adsorbed ammonium ions. Figure 3(b) shows the TG-DTA curve of the nanoparticles obtained using the  $\text{NH}_3$  (aq) ( $[\text{NH}_3] = 1$  mol/L). In this case, 24% of the

large weight loss caused by desorption of adsorbed  $\text{H}_2\text{O}$  was also observed below 400 K. The DTA curve had an exothermic peak around 535 K, and the temperature was close to that of Figure 4(a). Therefore, this DTA peak corresponds to the oxidation of organic molecules. The weight loss around this temperature was 2.4%. This value of the weight loss in Figure 3(b) was less than that in Figure 3(a). This result means that TIP molecules in the 1 mol/L of  $\text{NH}_3$  (aq) are more effectively hydrolyzed than those in the 1 mol/L of  $\text{NH}_3$  (aq). Furthermore, the slight decrease in mass corresponded to desorption of ammonium ions and the surface OH groups, as discussed in Figure 3(a). Accordingly, the hydrolysis reaction of titanium alkoxides proceeded more effectively at higher concentrations of  $\text{NH}_3$  (aq).

### 3.2. Investigation of Dispersion Stability and Formation Process of Sols by Using UV-VIS Absorption Spectra Measurements.

To examine dispersed state of particles in the obtained sols, UV-VIS absorption spectra were measured as presented in Figure 4. When the  $[\text{NH}_3]$  was 0.05 mol/L, the value of optical absorbance at 400 nm was 0.35. In this case, the obtained solution was a slightly opaque sol. Then, the observed optical absorbance corresponded to scattering of light. Furthermore, when wavelength decreased from 400 nm to 320 nm, the optical absorbance increased from 0.35 to 3.00. This increase of the optical absorbance corresponds to the electron transition between band gap of  $\text{TiO}_2$ . In general, a charge transfer transition between  $\text{O}^{2-}$  ion and  $\text{Ti}^{4+}$  ion also causes optical absorption in this wavelength range [20]. Figures 4(f)–4(h) show optical absorption spectra of isopropanol solution of TIP whose concentrations were, respectively, 1 mol/L, 0.1 mol/L, and 0.01 mol/L. According to Figure 4(f), the absorption edge of the charge transfer transition was around 355 nm when the concentration of the isopropanol solution of TIP was 1 mol/L. As shown in Figures 4(f)–4(h), with decreasing the TIP concentration in the solution from 1 mol/L to 0.01 mol/L, the wavelength of the absorption edge shifted from 355 nm to a shorter wavelength. Because the maximum concentration of TIP in the obtained sol was 0.05 mol/L, the absorption edge, which corresponded to the charge transfer, was expected to be less than 355 nm. The strong absorption around 375 nm in Figure 4(a) accordingly corresponded to the band gap transition of electrons in  $\text{TiO}_2$ . When the  $[\text{NH}_3]$  were greater than 0.1 mol/L, the optical absorbance at 400 nm was less than 0.05. Therefore, the obtained sol was almost transparent for visible light, and the scattering of light by the particles in the sol was slight. Therefore, transparent and homogeneous sols without precipitate are obtainable merely by heating the mixture of ethylene glycol solution of TIP and  $\text{NH}_3$  (aq). Furthermore, the wavelength of the absorption edge decreased with the increase of the  $[\text{NH}_3]$ , and the wavelengths remained longer than 360 nm. The strong optical absorption corresponded to the band gap electron transition of  $\text{TiO}_2$  and indicated the formation of  $\text{TiO}_2$  particles in the solution during the heating process.

To examine the formation process of titanium oxide nanoparticles in the TIP solution, we examined change

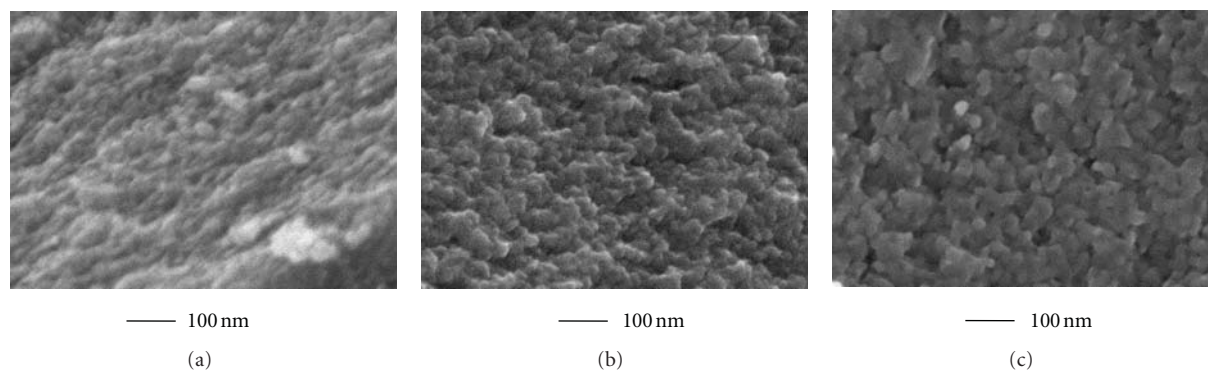


FIGURE 2: FE-SEM images of the titanium oxide particles obtained by heating the mixture of ethylene glycol solution of TIP and  $\text{NH}_3$  (aq) at 368 K for 24 h. The  $[\text{NH}_3]$  values were (a) 0.1 mol/L, (b) 0.5 mol/L, and (c) 1 mol/L.

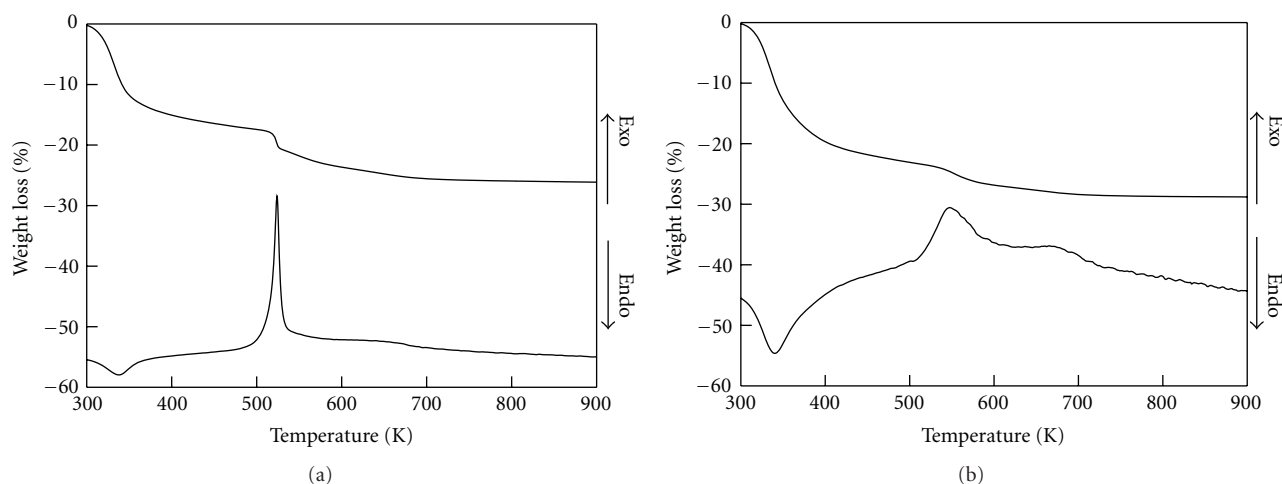


FIGURE 3: TG-DTA curves of the titanium oxide nanoparticles obtained by heating the mixture of ethylene glycol solution of TIP and  $\text{NH}_3$  (aq). The  $[\text{NH}_3]$  values were (a) 0.1 mol/L and (b) 1 mol/L.

of UV-VIS absorption spectra of the solution during the heating process. Figure 5 portrays the UV-VIS absorption spectra of the sols obtained by heating the mixture of ethylene glycol solution of TIP and  $\text{NH}_3$  (aq) at 368 K. As presented in Figure 5(a), when the heating time was 0 h, that is, before the heat treatment, value of the optical absorbance at 400 nm was 0.52. The obtained solution was an opaque sol. Then, the observed optical absorbance corresponded to scattering of light. The optical absorbance increased from 0.35 to 3.00 for wavelengths of 400–320 nm. This spectrum resembled that portrayed in Figure 2(g). Therefore, this increase of the optical absorbance corresponds to the charge transfer transition between  $\text{O}^{2-}$  ion and  $\text{Ti}^{4+}$  ion. As presented in Figure 5(b), the optical absorbance at 400 nm of the solution that had been heated for 1 h was 0.01. Accordingly, the obtained solution was almost transparent in the visible light wavelength range. The absorption edge was 344 nm. When heating times were longer than 1 h, the optical absorption at 400 nm remained almost 0, which indicates that the solution was transparent and the clear sol was obtained. The absorption edge of the steep increase of absorbance shifted from 344 nm to 359 nm when the heating

time increased from 0 h to 24 h. This shift of the wavelength of the absorption edge indicated the formation of anatase  $\text{TiO}_2$  lattice. If the shift of the adsorption edge was caused by decrease of the concentration of TIP in the solution, the wavelength of the charge transfer absorption would shift to shorter wavelength with increase of the heating time. The band gap energy, which corresponds to the wavelength of the absorption edge, depends on the size of nanoparticles by the quantum size effect. Therefore, the shift of the absorption edge signifies formation of titanium oxide and change of its particle sizes. Accordingly, the heating of the mixture of ethylene glycol solution of TIP and  $\text{NH}_3$  (aq) at 368 K for more than 1 h was sufficient to obtain the transparent and homogeneous sol of titanium oxide nanoparticles.

*3.3. Dye Adsorption Characteristics of the Titanium Oxide Nanoparticles Obtained by Hydrolysis Reaction of Ethylene Glycol Solution of TIP.* To examine the surface properties of the obtained titanium oxide nanoparticles, the  $\text{N}_2$  adsorption isotherms at 77 K were measured, and the BET-specific surface area was estimated. Figure 6 shows  $\text{N}_2$  adsorption isotherms of the titanium oxide nanoparticles obtained with

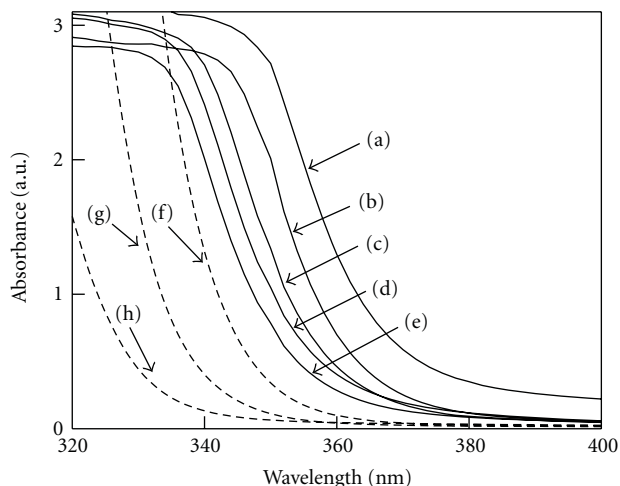


FIGURE 4: UV-VIS absorption spectra of the sols obtained by heating the mixture of ethylene glycol solution of TIP and  $\text{NH}_3$  (aq) at 368 K for 24 h. The solid line shows the spectra of the obtained sols. The  $\text{NH}_3$  (aq) concentrations were (a) 0.05 mol/L, (b) 0.1 mol/L, (c) 0.2 mol/L, (d) 0.5 mol/L, and (e) 1 mol/L. The broken lines show spectra of the isopropanol solution of TIP. The TIP concentrations of the solutions were (f) 1 mol/L, (g) 0.1 mol/L, and (h) 0.01 mol/L.

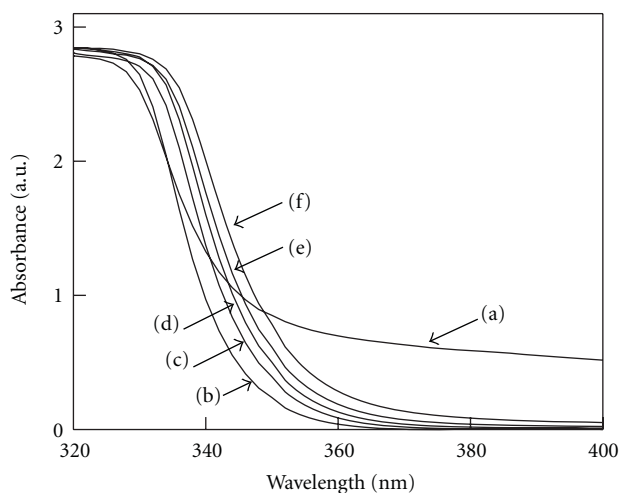


FIGURE 5: UV-VIS absorption spectra of the mixture of ethylene glycol solution of TIP and  $\text{NH}_3$  (aq) ( $[\text{NH}_3]=1$  mol/L). The heating temperature was 368 K. The heating times were the following: (a) 0 h (before heating), (b) 1 h, (c) 3 h, (d) 6 h, (e) 12 h, and (f) 24 h.

0.1 mol/L and 1 mol/L of the  $\text{NH}_3$  (aq). Additionally, a  $\text{N}_2$  adsorption isotherm of the conventional anatase  $\text{TiO}_2$  particles obtained by heating the mixture of TIP and  $\text{H}_2\text{O}$  at 368 K for 24 h is also shown in Figure 6. Both  $\text{N}_2$  adsorption isotherms obtained with the  $\text{NH}_3$  aqueous solutions belong to the type I isotherms defined by IUPAC. The  $\text{N}_2$  adsorption isotherm of the conventional anatase  $\text{TiO}_2$  particles belongs to the type IV isotherm, and the hysteresis loop can be classified to the type H2 [21]. The  $\text{N}_2$  adsorption isotherms of the titanium oxide nanoparticles were analyzed by using BJH method to estimate the average pore sizes and the total

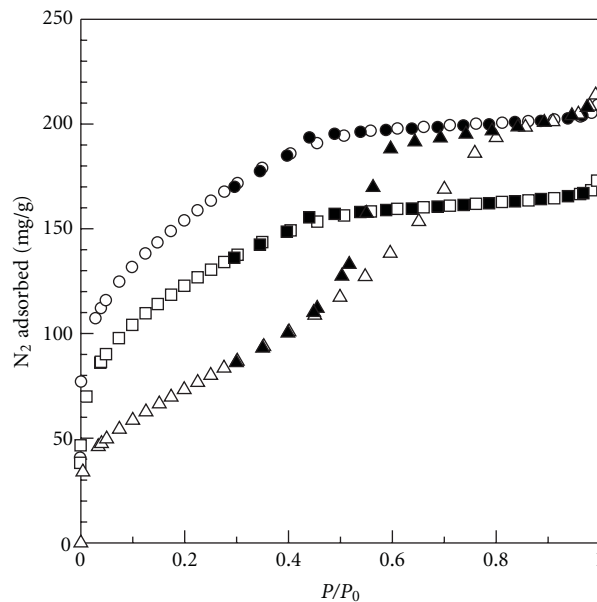


FIGURE 6:  $\text{N}_2$  adsorption isotherms of the titanium oxide nanoparticles obtained by heating the mixture of ethylene glycol solution of TIP and  $\text{NH}_3$  (aq) at 77 K.  $\circ$ ,  $\bullet$ : adsorption and desorption isotherms of  $[\text{NH}_3]=1$  mol/L.  $\square$ ,  $\blacksquare$ : adsorption and desorption isotherms of  $[\text{NH}_3]=0.1$  mol/L.  $\triangle$ ,  $\blacktriangle$ : adsorption and desorption isotherms of particles obtained by heating the mixture of TIP and  $\text{H}_2\text{O}$  at 368 K for 24 h.

pore volume. The  $\text{N}_2$  adsorption isotherms were analyzed using the Brunauer-Emmett-Teller (BET) equation, allowing us to obtain the specific surface area of the titanium oxide nanoparticles ( $S_{\text{BET}}$ ). The results of calculation were indicated in Table 1. When the  $[\text{NH}_3]$  values were 0.1 mol/L and 1 mol/L, the  $S_{\text{BET}}$  values were, respectively,  $358 \text{ m}^2/\text{g}$  and  $445 \text{ m}^2/\text{g}$ . With the higher concentration of  $\text{NH}_3$  (aq), coordination of  $\text{NH}_3$  molecules to  $\text{Ti}^{4+}$  ions inhibited rapid growth and aggregation of the nanoparticles so that higher specific surface area were achieved. However, the  $S_{\text{BET}}$  value of the anatase  $\text{TiO}_2$  particles obtained by heating the mixture of TIP and  $\text{H}_2\text{O}$  was  $214 \text{ m}^2/\text{g}$ . Accordingly, the titanium oxide nanoparticles obtained using the reaction between the ethylene glycol solution of TIP and  $\text{NH}_3$  (aq) had quite large  $S_{\text{BET}}$  values compared to those particles obtained using the conventional hydrolysis reaction of TIP. As, shown in the Table 1, the total pore volumes of the titanium oxide nanoparticles obtained with 0.1 mol/L and 1 mol/L of  $\text{NH}_3$  aqueous solutions were  $0.12 \text{ cm}^3/\text{g}$  and  $0.13 \text{ cm}^3/\text{g}$ , respectively, and they had very close values. The average pore sizes of the nanoparticles obtained with the 0.1 mol/L of  $\text{NH}_3$  (aq) were larger than those obtained with the 1 mol/L of  $\text{NH}_3$  (aq). Both of the average pore sizes were smaller than 2 nm so that the nanoparticles obtained with  $\text{NH}_3$  (aq) were microporous materials. On the other hand, the average pore size of the anatase  $\text{TiO}_2$  particles obtained by heating the mixture of TIP and  $\text{H}_2\text{O}$  was 4.67 nm. Accordingly, the obtained anatase  $\text{TiO}_2$  was a mesoporous material. The dependence of the porosity and the pore size on the  $\text{NH}_3$

TABLE 1: The BET specific surface areas of the nanoparticles obtained by heating the mixture of the ethylene glycol solution of TIP and the  $\text{NH}_3$  aqueous solution. Average pore diameter and total pore volume were estimated by using the BJH method to the  $\text{N}_2$  adsorption isotherms shown in Figure 6.

The solution added to ethyleneglycol solution of TIP	$[\text{NH}_3] = 0.1 \text{ M}$	$[\text{NH}_3] = 1 \text{ M}$	$\text{H}_2\text{O}$
$S_{\text{BET}}$	$358 \text{ m}^2/\text{g}$	$445 \text{ m}^2/\text{g}$	$214 \text{ m}^2/\text{g}$
Average pore diameter	1.34 nm	1.17 nm	4.67 nm
Total pore volume	$0.12 \text{ cm}^3/\text{g}$	$0.13 \text{ cm}^3/\text{g}$	$0.25 \text{ cm}^3/\text{g}$

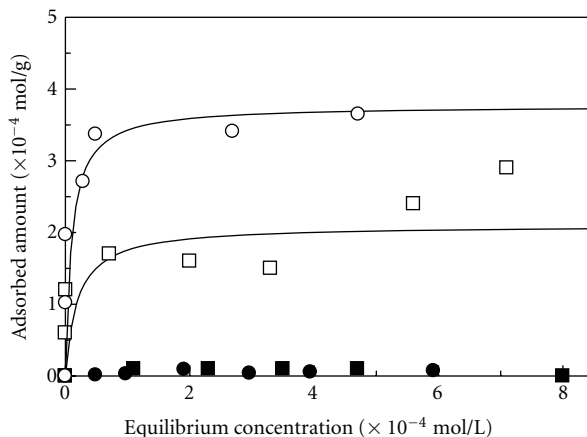


FIGURE 7: Adsorption isotherms of dye molecules on the titanium oxide nanoparticles in aqueous solution of dye. Aqueous solutions of the dye molecules were the following:  $\circ$ , methylene blue;  $\square$ , crystal violet;  $\bullet$ , Evans blue;  $\blacksquare$ , eosin Y. The titanium oxide nanoparticles were prepared using the aqueous solution having  $[\text{NH}_3]$  of 1 mol/L.

(aq) concentration reflected the difference of the hydrolysis reaction in the solutions.

Adsorption isotherms of dye molecules were measured to investigate the interaction between the dye molecules and the titanium oxide nanoparticle surfaces. Figure 7 presents adsorption isotherms of dye molecules on the titanium oxide nanoparticles obtained at  $[\text{NH}_3]=1 \text{ mol/L}$ . The adsorption isotherms of the cationic dye molecules of methylene blue and crystal violet on the obtained titanium oxide nanoparticles are shown, respectively, as open circles and open squares. The black line shows the result of least-square curve-fitting based on Langmuir equation, which fits the experimental data very well. The saturated adsorbed amount of methylene blue and crystal violet was, respectively,  $3.59 \times 10^{-4} \text{ mol/g}$  and  $2.02 \times 10^{-4} \text{ mol/g}$ . The adsorption isotherms of the anionic dye molecules of eosin Y and Evans blue on the titanium oxide nanoparticles are shown, respectively, as closed squares and closed circles. The saturated adsorbed amounts of eosin Y and Evans blue, as calculated from the Langmuir plots, were, respectively,  $8.25 \times 10^{-6} \text{ mol/g}$  and  $6.91 \times 10^{-6} \text{ mol/g}$ . Accordingly, the saturated adsorbed amounts of the anionic dye molecules were less than 1/50 of those of the cationic dye molecules. Highly selective adsorption of the cationic dye molecules was observed.

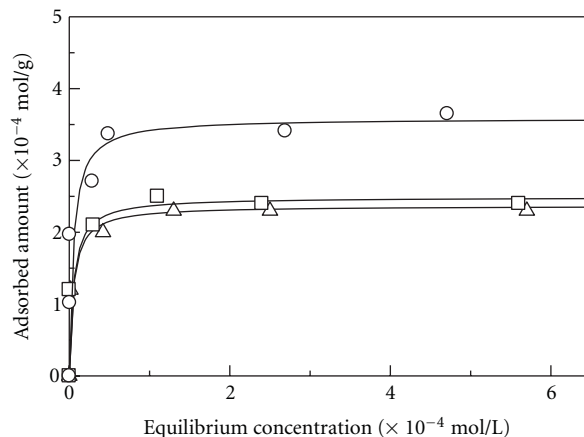


FIGURE 8: Adsorption isotherms of methylene blue on the titanium oxide nanoparticles in aqueous solution of dye. The  $\text{NH}_3$  aqueous solutions concentrations used to prepare the titanium oxide nanoparticles were the following:  $\circ$ , 1 mol/L;  $\square$ , 0.2 mol/L;  $\triangle$ , 0.1 mol/L.

To examine more details of the selective adsorption of the cationic dye molecules, the adsorption isotherms of methylene blue, which is a cationic dye molecule, were measured as presented in Figure 8. The adsorbents were titanium oxide nanoparticles prepared by using  $\text{NH}_3$  (aq) whose concentrations were 0.1 mol/L, 0.2 mol/L, and 1 mol/L. The saturated adsorbed amounts estimated by using the Langmuir plot were, respectively,  $2.37 \times 10^{-4} \text{ mol/g}$ ,  $2.49 \times 10^{-4} \text{ mol/g}$ , and  $3.59 \times 10^{-4} \text{ mol/g}$ . The saturated adsorbed amounts corresponded to  $S_{\text{BET}}$  values of the titanium oxide nanoparticles.

Figure 9 shows adsorption isotherms of Evans blue, which is an anionic dye molecule. The saturated adsorbed amounts of Evans blue molecules of the nanoparticles were less than  $2.5 \times 10^{-5} \text{ mol/g}$ . According to the results presented in Figures 8 and 9, the cationic dye molecules interacted strongly with the surface of the titanium oxide nanoparticles obtained by heating the mixtures of ethylene glycol solution of TIP and  $\text{NH}_3$  (aq). As presented in Figure 1(d), when the  $[\text{NH}_3]$  value was 1 mol/L, the obtained nanoparticles were mixture of anatase  $\text{TiO}_2$  and layered titanate. In general, a layered titanate structure shows the cationic ion exchange property. Therefore, an enhanced adsorption towards the cationic dye molecules on the nanoparticles

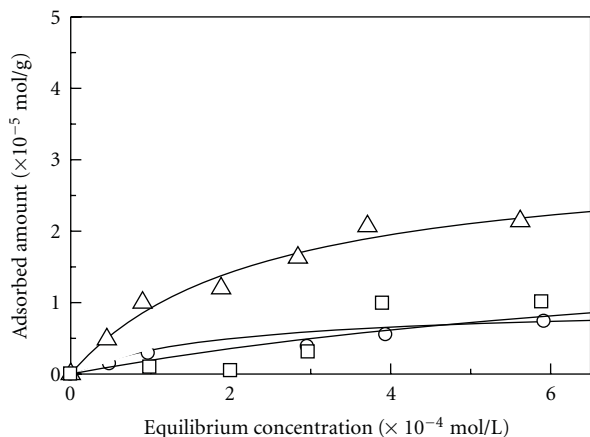


FIGURE 9: Adsorption isotherms of Evans blue on the titanium oxide nanoparticles in aqueous solution of dye. The concentrations of  $\text{NH}_3$  (aq) used to prepare the titanium oxide nanoparticles were the following:  $\circ$ , 1 mol/L;  $\square$ , 0.2 mol/L; and  $\triangle$ , 0.1 mol/L.

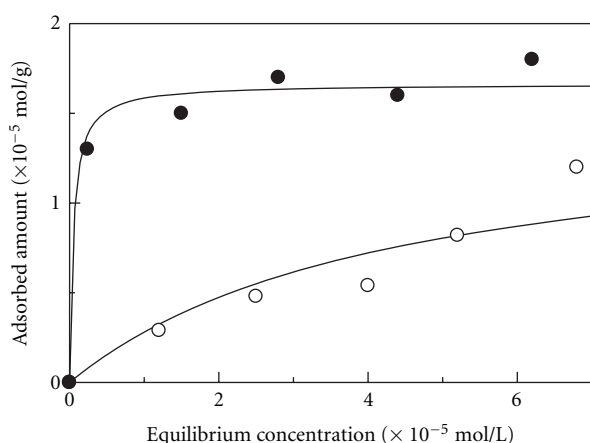


FIGURE 10: Adsorption isotherms of dye molecules on titanium oxide nanoparticles in aqueous solution of dye. The dye molecules were the following:  $\circ$ , methylene blue and  $\bullet$ , Evans blue. Titanium oxide nanoparticles were prepared by heating the mixture of TIP and  $\text{H}_2\text{O}$  at 368 K for 24 h.

corresponded to the presence of layered titanic acid structure in the obtained nanoparticles. On the other hand, although the XRD peaks of the nanoparticles prepared at  $[\text{NH}_3] = 0.1$  mol/L as presented in Figure 1(a) can be assigned only to anatase  $\text{TiO}_2$ , the obtained nanoparticles also showed the enhanced adsorption towards the cationic dye molecules. In this case, the layered titanic acid particles with very low degree of crystallization were included in the obtained nanoparticles so that the presence of the layered titanic acid phase cannot be detected by XRD. To examine the above consideration, the adsorption characteristics of conventional anatase  $\text{TiO}_2$  particles, the dye adsorption isotherms of the particles were presented in Figure 10. The saturated adsorbed amounts of methylene blue and Evans blue were, respectively,  $1.50 \times 10^{-5}$  mol/g and  $1.66 \times 10^{-5}$  mol/g. In

this case, the adsorbed amount of Evans blue, an anionic dye molecule, was larger than that of methylene blue, a cationic dye molecule. This adsorption behavior was opposite to the titanium nanoparticles obtained from the ethylene glycol solution of TIP and  $\text{NH}_3$  aqueous solution. Accordingly, the positively charged sites on the anatase particles such as  $\text{Ti}^{4+}$  ions played an important role in the adsorption of Evans blue molecules. Therefore, the adsorption behavior of the dye molecules depends strongly on the surface characteristics. Results show that the selective adsorption of the cationic dye molecules did not correspond to the anatase  $\text{TiO}_2$  structure. The layered titanic acid structure is expected to play an important role in the selective adsorption of the cationic dye molecules. The hydrolysis reaction with a sufficient amount of  $\text{NH}_3$  aqueous solution enabled formation of a composite of layered titanic acid structure and anatase  $\text{TiO}_2$ , and it is considered that the structure contributed to the selective dye adsorption characteristics.

#### 4. Conclusion

Transparent and stable sols of titanium oxide nanoparticles were obtained by heating a mixture of ethylene glycol solution of TIP and  $\text{NH}_3$  aqueous solution at 368 K for 24 h. The concentration of  $\text{NH}_3$  aqueous solution affected the structure of the obtained titanium oxide nanoparticles. When the concentration of  $\text{NH}_3$  aqueous solution was 0.1 mol/L, the obtained nanoparticles were assigned to anatase  $\text{TiO}_2$  according to the XRD pattern. When the concentration was higher than 0.2 mol/L, a mixture of anatase  $\text{TiO}_2$  nanoparticles and layered titanic acid nanoparticles was obtained. The coordination of ethylene glycol and  $\text{NH}_3$  molecules to  $\text{Ti}^{4+}$  ions played an important role in the formation of titanium oxide nanoparticles and their homogeneous dispersion in the sol. The obtained titanium oxide nanoparticles had a large specific surface area, which was larger than  $350 \text{ m}^2/\text{g}$  because the aggregation of their nanoparticles was prevented by the coordination of  $\text{NH}_3$  and ethylene glycol molecules. The obtained titanium oxide nanoparticles indicated an enhanced adsorption towards the cationic dye molecules. The selective adsorption corresponded to presence of the layered titanic acid on the nanoparticles. The high specific surface area also played an important role for the selective adsorption of the cationic dye molecules. Accordingly, the hydrolysis reaction of TIP with ethylene glycol and  $\text{NH}_3$  enabled us to obtain stable sols of anatase  $\text{TiO}_2$  and layered titanic acid nanoparticles with highly homogeneous dispersion. Furthermore, the obtained nanoparticles showed unique adsorption characteristics.

#### Acknowledgment

This work was supported by the Grant-in-Aid for Scientific Research (C) of the Japan Society for the Promotion of Science.

## References

- [1] A. Alem, H. Sarpoalaky, and M. Keshmiri, "Titania ultrafiltration membrane: preparation, characterization and photocatalytic activity," *Journal of the European Ceramic Society*, vol. 29, no. 4, pp. 629–635, 2009.
- [2] K. Lv, J. Yu, L. Cui, S. Chen, and M. Li, "Preparation of thermally stable anatase TiO<sub>2</sub> photocatalyst from TiOF<sub>2</sub> precursor and its photocatalytic activity," *Journal of Alloys and Compounds*, vol. 509, no. 13, pp. 4557–4562, 2011.
- [3] C. Bechinger, S. Ferrere, A. Zaban, J. Sprague, and B. A. Gregg, "Photoelectrochromic windows and displays," *Nature*, vol. 383, no. 6601, pp. 608–610, 1996.
- [4] E. Topoglidis, A. E. G. Cass, G. Gilardi, S. Sadeghi, N. Beaumont, and J. R. Durrant, "Protein adsorption on nanocrystalline TiO<sub>2</sub> films: an immobilization strategy for bioanalytical devices," *Analytical Chemistry*, vol. 70, no. 23, pp. 5111–5113, 1998.
- [5] M. R. Hoffmann, S. T. Martin, W. Choi, and D. W. Bahnemann, "Environmental applications of semiconductor photocatalysis," *Chemical Reviews*, vol. 95, no. 1, pp. 69–96, 1995.
- [6] K. M. Lee, V. Suryanarayanan, J. H. Huang, K. R. J. Thomas, J. T. Lin, and K. C. Ho, "Enhancing the performance of dye-sensitized solar cells based on an organic dye by incorporating TiO<sub>2</sub> nanotube in a TiO<sub>2</sub> nanoparticle film," *Electrochimica Acta*, vol. 54, no. 16, pp. 4123–4130, 2009.
- [7] W. J. Tseng and K. C. Lin, "Rheology and colloidal structure of aqueous TiO<sub>2</sub> nanoparticle suspensions," *Materials Science and Engineering A*, vol. 355, no. 1-2, pp. 186–192, 2003.
- [8] U. G. Akpan and B. H. Hameed, "The advancements in sol-gel method of doped-TiO<sub>2</sub> photocatalysts," *Applied Catalysis A*, vol. 375, no. 1, pp. 1–11, 2010.
- [9] C. D. Jaeger and A. J. Bard, "Spin trapping and electron spin resonance detection of radical intermediates in the photodecomposition of water at TiO<sub>2</sub> particulate systems," *Journal of Physical Chemistry*, vol. 83, no. 24, pp. 3146–3152, 1979.
- [10] N. Sakai, R. Wang, A. Fujishima, T. Watanabe, and K. Hashimoto, "Effect of ultrasonic treatment on highly hydrophilic TiO<sub>2</sub> surfaces," *Langmuir*, vol. 14, no. 20, pp. 5918–5920, 1998.
- [11] B. O'Regan and M. Grätzel, "A low-cost, high-efficiency solar cell based on dye-sensitized colloidal TiO<sub>2</sub> films," *Nature*, vol. 353, no. 6346, pp. 737–740, 1991.
- [12] M. K. Nazeeruddin, A. Kay, I. Rodico et al., "Conversion of light to electricity by cis-X<sub>2</sub>bis(2,2'-bipyridyl-4,4'-dicarboxylate)ruthenium(II) charge-transfer sensitizers (X = Cl<sup>-</sup>, Br<sup>-</sup>, I<sup>-</sup>, CN<sup>-</sup>, and SCN<sup>-</sup>) on nanocrystalline titanium dioxide electrodes," *Journal of the American Chemical Society*, vol. 115, no. 14, pp. 6382–6390, 1993.
- [13] M. C. Rath, D. K. Palit, T. Mukherjee, and H. N. Ghosh, "Sensitization of TiO<sub>2</sub> nanoparticles in micro-emulsion by photoexcited dye molecules: a femtosecond transient absorption study," *Journal of Photochemistry and Photobiology A*, vol. 204, no. 2-3, pp. 209–216, 2009.
- [14] M. I. Zaki, G. A. H. Mekhemer, N. E. Fouad, T. C. Jagadale, and S. B. Ogale, "Surface texture and specific adsorption sites of sol-gel synthesized anatase TiO<sub>2</sub> nanoparticles," *Materials Research Bulletin*, vol. 45, no. 10, pp. 1470–1475, 2010.
- [15] N. Nakayama and T. Hayashi, "Preparation of TiO<sub>2</sub> nanoparticles surface-modified by both carboxylic acid and amine: dispersibility and stabilization in organic solvents," *Colloids and Surfaces A*, vol. 317, no. 1–3, pp. 543–550, 2008.
- [16] N. Uekawa, M. Suzuki, T. Ohmiya, F. Mori, Y. J. Wu, and K. Kakegawa, "Synthesis of rutile and anatase TiO<sub>2</sub> nanoparticles from Ti-peroxy compound aqueous solution with polyols," *Journal of Materials Research*, vol. 18, no. 4, pp. 797–803, 2003.
- [17] A. Singh and R. C. Mehrotra, "Novel heterometallic alkoxide coordination systems of polyols (glycols, di- and tri-ethanolamines) derived from the corresponding homometallic moieties," *Coordination Chemistry Reviews*, vol. 248, no. 1-2, pp. 101–118, 2004.
- [18] L. G. Hubert-Pfalzgraf, "Some aspects of homo and heterometallic alkoxides based on functional alcohols," *Coordination Chemistry Reviews*, vol. 178–180, no. 2, pp. 967–997, 1998.
- [19] M. Zhang, Z. Jin, J. Zhang et al., "Effect of annealing temperature on morphology, structure and photocatalytic behavior of nanotubed H<sub>2</sub>Ti<sub>2</sub>O<sub>4</sub>(OH)<sub>2</sub>," *Journal of Molecular Catalysis A*, vol. 217, no. 1-2, pp. 203–210, 2004.
- [20] M. R. Harrison, P. P. Edwards, and J. B. Goodenough, "A study of the Li<sub>1+x</sub>Ti<sub>2-x</sub>O<sub>4</sub> spinel system by diffuse-reflectance spectroscopy," *Journal of Solid State Chemistry*, vol. 54, no. 3, pp. 426–437, 1984.
- [21] S. J. Gregg and K. S. W. Sing, *Adsorption, Surface Area and Porosity*, Academic Press, London, UK, 2nd edition, 1982.

## Research Article

# Direct Vapor-Phase Bromination of Multiwall Carbon Nanotubes

Ilya Mazov,<sup>1</sup> Dmitry Krasnikov,<sup>1,2</sup> Andrey Stadnichenko,<sup>1</sup> Vladimir Kuznetsov,<sup>1</sup>  
Anatoly Romanenko,<sup>2,3</sup> Olga Anikeeva,<sup>2,3</sup> and Evgeniy Tkachev<sup>3</sup>

<sup>1</sup> Department of Physical Methods of Research, Boreskov Institute of Catalysis, Lavrentieva Avenue 5, Novosibirsk 630090, Russia

<sup>2</sup> Department of Thermodynamic Studies, Novosibirsk State University, Pirogova street 2, Novosibirsk 630090, Russia

<sup>3</sup> Department of Physics, Nikolaev Institute of Inorganic Chemistry, Lavrentieva Avenue 5, Novosibirsk 630090, Russia

Correspondence should be addressed to Ilya Mazov, ilya.mazov@gmail.com

Received 29 November 2011; Accepted 20 March 2012

Academic Editor: Angaiiah Subramania

Copyright © 2012 Ilya Mazov et al. This is an open access article distributed under the Creative Commons Attribution License, which permits unrestricted use, distribution, and reproduction in any medium, provided the original work is properly cited.

We present the simple procedure of the vapor-phase bromination of multiwall carbon nanotubes (MWNTs) at moderate temperatures. MWNTs with average diameter  $9 \pm 3$  nm were treated with Br<sub>2</sub> vapors at 250°C to produce Br-functionalized product. Transmission electron microscopy analysis was used to prove low damage of MWNT walls during bromination. X-ray photoelectron spectroscopy (XPS) and differential thermal analysis (DTA) were used to investigate chemical composition of the surface of initial and brominated nanotubes. The experimental results show that the structure of MWNTs is not affected by the bromination process and the total amount of Br-containing surface functions reaches 2.5 wt. %. Electrophysical properties of initial and brominated MWNTs were investigated showing decrease of conductivity for functionalized sample. Possible mechanism of the vapor-phase bromination via surface defects and oxygen-containing functional groups was proposed according to data obtained. Additional experiments with bromination of annealed low-defected MWNTs were performed giving Br content a low as 0.75 wt. % proving this hypothesis.

## 1. Introduction

Carbon nanotubes (CNTs) attract great attention in the last decade due to their remarkable mechanical, optical, and electrical properties. Usage of CNTs is strongly limited due to their high chemical inertness and insolubility in conventional organic solvents, thus preventing chemical interaction with other organic species or matrices of composite materials. Chemical functionalization of the surface of CNTs is important step for modification and fine tuning of their properties by enhancing of compatibility with other materials, grafting of various functional groups, and so forth [1, 2].

One of the most promising methods of CNT functionalization is introduction of halogen atoms of the CNT surface. Carbon-halogen bond can be easily modified using conventional methods of organic chemistry—such as reduction, alkylation, and hydroxylation. Due to relatively high chemical inertness of CNT surface, special technique should be used in order to react halogens with nanotubes, especially for low-reactive bromine. At the same time, bromination of CNTs is more preferable as compared with more easy

fluorination or chlorination due to higher reactivity of C-Br bond in further functionalization steps.

Several approaches were used for functionalization of carbon nanomaterials with halogens—for example, microwave- and plasma-assisted halogenation [3–5], radiation-induced chlorination and bromination [6, 7], bromination with Lewis acids [8], usage of liquid bromine or vapors at room temperature [9–11], or electrochemically generated Br<sub>2</sub> and Cl<sub>2</sub> [12]. Almost all of these methods require usage of special techniques or experimental methods. Here, we report simple way of synthesis of Br-modified multiwall carbon nanotubes produced by direct treatment in bromine vapors at elevated temperature. Bromine is covalently linked with the surface of carbon nanotubes with total Br amount 0.5 at. % or 2.5 wt. %.

## 2. Experimental

Initial MWNTs with specific surface area  $\sim 330 \pm 15$  m<sup>2</sup>/g were prepared by C<sub>2</sub>H<sub>4</sub> decomposition over FeCo catalyst at 700°C and were purified by reflux with HCl. Mean diameter

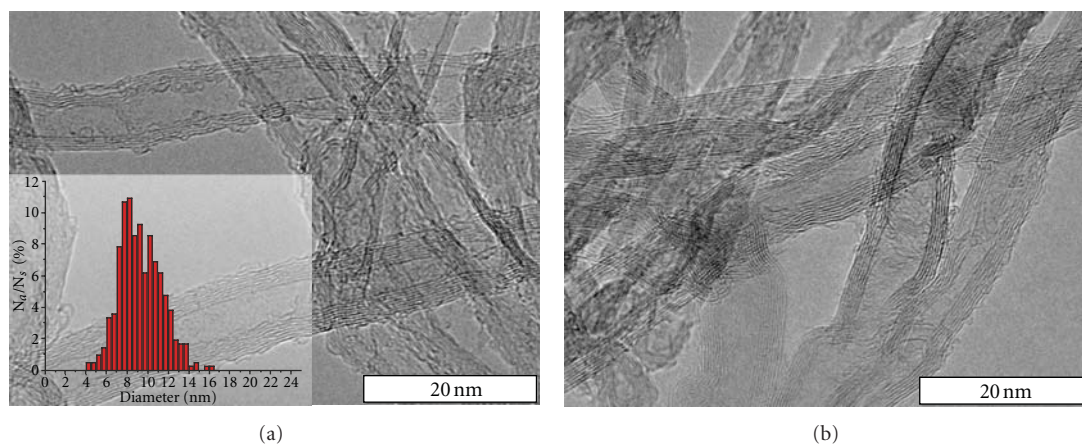


FIGURE 1: (a) High resolution TEM image of initial MWNTs with corresponding diameter distribution; (b) high resolution TEM image of the brominated sample, revealing no significant structure changes in nanotubes.

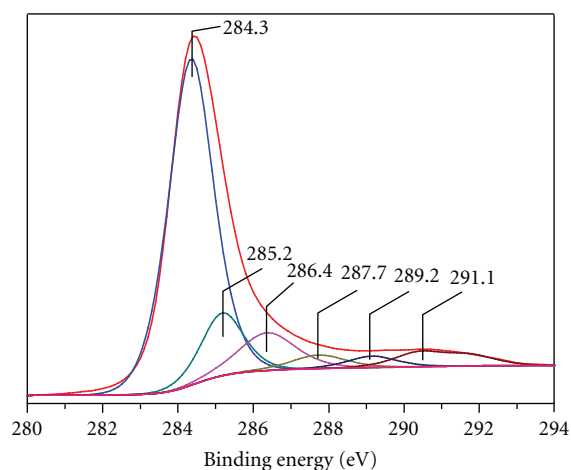


FIGURE 2: XPS C1s spectrum for both initial and brominated samples and its decomposition on individual peaks.

of MWNTs was statistically measured using TEM data and was  $9 \pm 3$  nm. Bromination was carried out at  $250^\circ\text{C}$  in an electrically heated glass reactor, connected to the flask with distilled bromine kept at  $80^\circ\text{C}$ . MWNTs were loaded in hot reactor filled with bromine vapors. After treatment of MWNTs with  $\text{Br}_2$  vapor, the reactor was washed with pure Ar flow and cooled to room temperature. Nanotubes were unloaded from reaction vessel and dried in vacuum ( $10^{-2}$  torr) at  $80^\circ\text{C}$  overnight. Bromine-treated MWNTs ( $\text{MWNT}^{\text{Br}}$ ) and pristine MWNTs ( $\text{MWNT}^{\text{ini}}$ ) were investigated using TEM, DTA, and XPS methods.

Additional comparative experiments by the bromination of nanotubes annealed at high temperature in pure Ar flow ( $2800^\circ\text{C}$ , see [13] for details) were performed. Annealed nanotubes possess perfect structure of graphene sheets and very low amount of structural and topological defects; thus this sample was used as comparative sample for elucidation of bromination mechanism.

### 3. Results and Discussion

Structure and morphology of initial and brominated MWNTs were investigated using scanning and transmission electron microscopy (see Figures 1(a) and 1(b)). No significant changes were observed for brominated sample, thus indicating that bromine treatment at moderate temperatures does not inflict damages in nanotube structure. EDX analysis was performed for agglomerates of nanotubes revealing 1.4–1.6 at. % of bromine.

Chemical composition of initial and brominated nanotubes was investigated using XPS technique. XPS survey spectra for  $\text{MWNT}^{\text{ini}}$  and  $\text{MWNT}^{\text{Br}}$  samples are shown of Figure 2. Spectrum of initial nanotubes shows peaks only from C1s (284.4 eV) and O1s (532.3 eV) with oxygen content  $\sim 1.35$  at. %. Spectrum of brominated nanotubes reveals peaks from C1s, O1s, Br3d (70.1 eV), Br3p (183.7 eV) with total oxygen and bromine content  $\sim 1.28$  at. % and 0.41 at. %, correspondingly. Note that total oxygen content decreases after bromination in contrast to observed elsewhere [3] for the process of CNT bromination in water media by microwaves. Slight decrease of oxygen content can be attributed to the substitution of oxygen atoms in carboxylic functional groups by bromine with no parallel reactions such as Br substitution by water due to nucleophilic mechanism.

High-resolution XPS spectrum of C1s shown on Figure 2 was fitted using Gauss and Lorentz peaks and Doniach-Sunjic curve deconvolution [14]. Peak form analysis was performed after Shirley background subtraction [15]. Following main components are observed: (1) main peak from  $sp^2$ -hybridized C atoms (main grapheme-like structure of the nanotube) located at 284.4 eV (80.5 at. %) with corresponding shake-up peak at 290.7 eV (6.0 at. %), (2) signal from  $sp^3$ -hybridized carbon atoms at 285.1 eV (3.1 at. %), (3) peak from carbon atoms in C–O or C–Br functional groups located at 286.2 eV (3.7 at. %), and (4) peak from carbonyl and carboxyl functions at 287.8 eV (6.7 at. %). Note that vapor-phase bromination of MWNTs does not result in any significant changes of the form and intensity of C1s line, which may be attributed to low structural changes

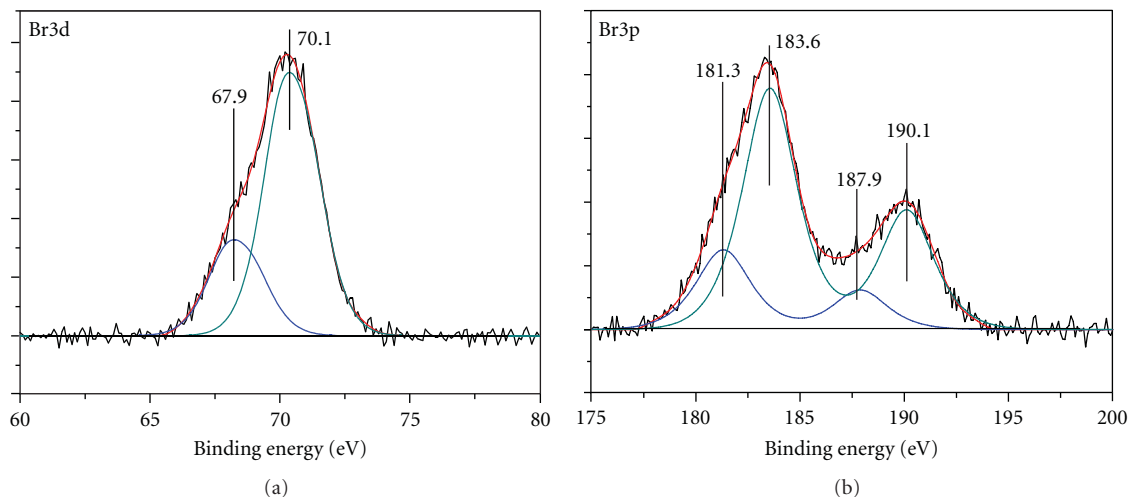


FIGURE 3: Decomposition of Br3d line (a) and Br3p line (b) for MWNT<sup>Br</sup> sample.

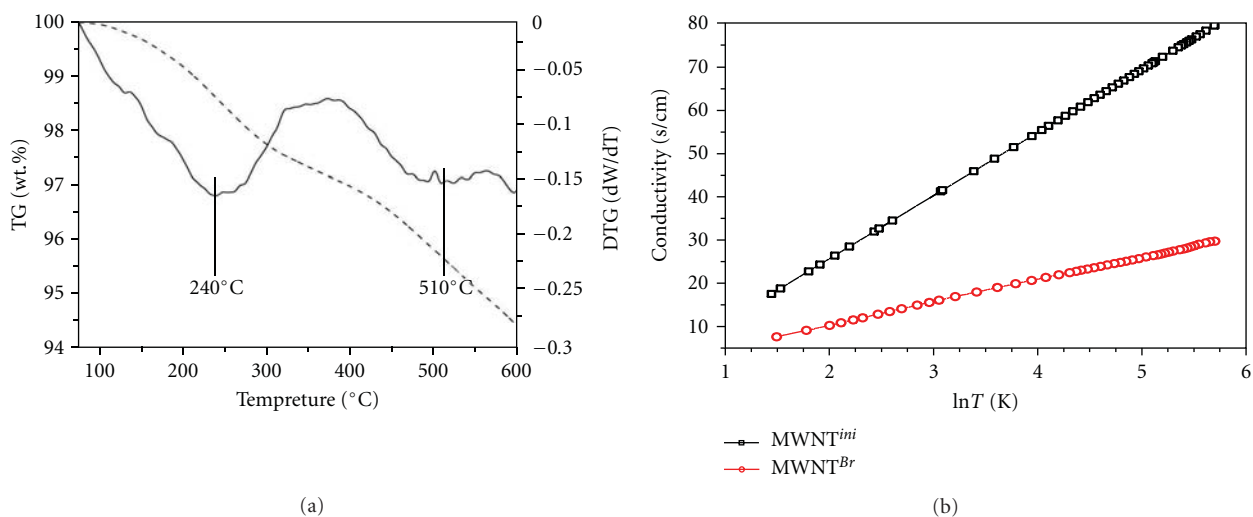


FIGURE 4: (a) Thermal analysis data for MWNT<sup>Br</sup> sample in nitrogen atmosphere at 10 K/min (solid line represents differential thermal data, dashed line represents thermogravimetric data); (b) temperature dependencies of electrical conductivity for initial and brominated MWNTs.

of nanotubes and substitution mechanism of bromination through carboxylic surface groups (peak 3 at 286.4 eV), which corresponds to TEM data on the low modification of CNT structure.

High-resolution XPS spectra for Br3d and Br3p lines are shown in Figure 3. Br3d spectrum (Figure 3(a)) is composed of two components with energies typical for covalently bonded Br atoms (70.1 eV, C–Br bonds) and negatively charged Br<sup>-</sup> species (67.9 eV), which are most probably absorbed bromine anions of bromine salts of metal catalyst residues. The ratio between C–Br and Br<sup>-</sup> components is near to 3:1. The Br3p spectrum shown on Figure 3(b) is composed of two main lines (Br3p 1/2 and Br3p 3/2), each one of them can be decomposed to two components,

corresponding to C–Br bonds and Br<sup>-</sup> species on the surface of nanotubes.

Differential thermal analysis data for MWNT<sup>Br</sup> in nitrogen atmosphere are shown on Figure 4(a). First decomposition of surface species proceeds between 100 and 350°C with maximum decomposition temperature at ~240°C. This value is higher than temperature of desorption of physically absorbed Br<sub>2</sub>, which was most probably removed during vacuum treatment after bromination and is close to that observed elsewhere for microwave-brominated DWNTs [3] and can be associated to decomposition of C–Br bonds. The second decomposition step occurs at 400–600°C with major peak at ~510°C, corresponding to possible dehydrobromination of functionalized nanotubes. Similar TGA

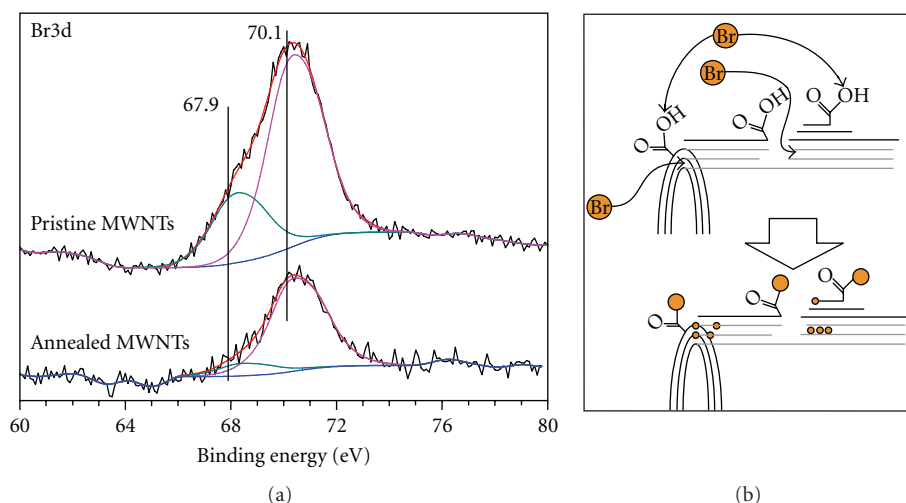


FIGURE 5: (a) High-resolution spectrum (Br3d) for initial and annealed carbon nanotubes. (b) Schematic of the Br interaction with surface groups of carbon nanotube.

behavior of brominated nanotubes was observed elsewhere and was linked to double-step dehydrobromination process with formation of allylic species on the MWNT surface [16].

According to TGA data total weight loss due to decomposition and desorption of surface species from brominated sample of nanotubes is close to 5.5 wt. % which is reasonably close to the value of Br content determined by means of XPS technique (2.5 wt. %) taking into consideration that desorption may proceed not only for individual bromine atoms but for C–Br-containing clusters, increasing total weight loss. Thus density of Br-containing species on the surface of MWNTs can be estimated as  $0.6\text{--}0.7\text{ nm}^{-2}$ . This value is close to the surface density of carboxylic groups for initial nanotubes determined by XPS and Boehm acid-base titration (not shown here).

*Electrical conductivity measurements* were performed for both initial and brominated samples. MWNT powder was pressed in the glass ampoule with silver contacts until the value of conductivity reached saturation. Electrophysical parameters were measured by four-probe technique successfully used earlier for investigation of various nanocarbon materials [17]. Temperature dependencies of electrical conductivity for initial and brominated sample are shown on Figure 4(b). Bromination of carbon nanotubes results in significant decrease of the electrical conductivity—sample  $\text{MWNT}^{\text{ini}}$  shows conductivity value  $20\text{--}80\text{ s/cm}$  depending on the temperature, and the sample  $\text{MWNT}^{\text{Br}}$  shows  $\sigma$  value in the range  $7\text{--}25\text{ s/cm}$  (Figure 4(b)).

Bromine atoms act as acceptors of electrons resulting in change of the density of current carriers in surface layers of the nanotube thus decreasing electrical conductivity of the sample. Moreover, the slope of the temperature dependence curves changes with functionalization of the surface which is attributed to the changes in the mechanism of electrical conductivity. Untreated nanotubes possess logarithmic temperature dependence corresponding to two-dimensional quantum corrections to conductivity (see [18] for details),

and brominated MWNTs show exponential temperature dependence of conductivity which can be described within theory of Coulomb blockade or quasi one-dimensional variable range hopping conductivity with variable length of hops between localized states one-dimensional hopping conductivity or Coulomb gap conductivity [19]. Such changes occur due to changes of current carriers density on the Fermi level due to interaction with bromine.

*Possible Mechanism of MWNT Bromination.* Decrease of the electrical conductivity is related with the bromination mechanism which can be described in the following way. Initial MWNTs possess structural defects on their surface—such as holes in graphene layers and nanosized curved graphitic sheets. Such structural defects have higher concentration of carboxylic groups and higher reactivity as compared with intact inner walls of nanotubes and react with bromine vapors according to following general reaction:



Hydrogen bromide can further react with unsaturated bonds situated on defect areas of nanotubes:



Bromination of annealed nanotubes results in decrease of the Br content on the surface of MWNTs as determined by XPS: 0.15 at. % for annealed nanotubes versus 0.5 at. % for untreated nanotubes (Figure 5(a)). The reason for this may be lower amount of structural and topological defects on the surface of annealed sample. Perfect graphene layers, that is, nanotube walls, are less able to react with bromine vapors at moderate temperatures. The same behavior is known for single-wall carbon nanotubes which have more perfect structure than multiwall nanotubes. In the case of absence of “dangling bonds,” curved graphitic layers or holes in the

nanotube walls, the reaction between halogen molecule and the surface of nanotube is strongly impeded. Formation of covalent bond between halogen and carbon layer proceeds with partial transition of electron density to the halogen from conjugated  $\pi$ -system of carbon atoms with subsequent change of the hybridization state of carbon from  $sp^2$  to  $sp^3$ . This process is energetically unfavorable in the case of perfect structure of brominated objects—that is, single-wall nanotubes or graphitized annealed nanotubes.

Another way of interaction of pristine MWNTs with bromine vapors is formation of “intercalate-like” structures with Br atoms between tangled graphene layers or Br chemisorption on the defective areas of nanotubes (Figure 5(b)). Both these types of linked Br atoms are seen on the high-resolution XPS spectrum for the sample MWNT<sup>Br</sup>. Low-defective annealed MWNT sample shows lower amount of total bonded bromine and higher content of covalently linked Br atoms. Thus it allows one to conclude that the bromination of MWNTs proceeds via interaction with surface defects and functional groups of carbon nanotubes.

#### 4. Conclusions

Vapor-phase reaction with bromine vapors at moderate temperature was successfully used for dry synthesis of Br-functionalized multiwall carbon nanotubes with overall bromine content  $\sim 2.5$  wt. %. Bromine is covalently bonded to the surface of the nanotube and no structural changes are observed with XPS, TEM, and SEM methods. Amount of Br-containing groups corresponds to that for carboxylic groups of initial nanotubes, thus possible mechanism of bromination can be formation of bromoanhydride-like functional groups.

Investigation of electrophysical properties of brominated nanotubes reveals significant changes in the conductivity due to interaction of Br atoms with the surface of the nanotube and consecutive changes in the current carries density on the Fermi level.

Br-functionalized carbon nanotubes can be further used for design of tailor-made materials using approaches of organometallic synthesis.

#### Acknowledgments

This work was supported by RFBR Grant no. 11-03-00351, ISTC Project no. 1708-B and Russian FASI Projects no. 16.740.11.0016, and no. 16.740.11.0146.

#### References

- [1] P.-C. Ma, N. A. Siddiqui, G. Marom, and J. K. Kim, “Dispersion and functionalization of carbon nanotubes for polymer-based nanocomposites: a review,” *Composites A*, vol. 41, no. 10, pp. 1345–1367, 2010.
- [2] J. K. Kim, *Carbon Nanotubes for Polymer Reinforcement*, CRC Press, 2011.
- [3] J. F. Colomer, R. Marega, H. Traboulsi, M. Meneghetti, G. van Tendeloo, and D. Bonifazi, “Microwave-assisted bromination of double-walled carbon nanotubes,” *Chemistry of Materials*, vol. 21, no. 20, pp. 4747–4749, 2009.
- [4] J. F. Friedrich, S. Wettmarshausen, S. Hanelt et al., “Plasma-chemical bromination of graphitic materials and its use for subsequent functionalization and grafting of organic molecules,” *Carbon*, vol. 48, no. 13, pp. 3884–3894, 2010.
- [5] S. C. Ray, C. W. Pao, H. M. Tsai et al., “Electronic structures and bonding properties of chlorine-treated nitrogenated carbon nanotubes: X-ray absorption and scanning photoelectron microscopy studies,” *Applied Physics Letters*, vol. 90, no. 19, Article ID 192107, 2007.
- [6] V. A. Volodina, A. A. Kozlovskii, S. I. Kuzina, and A. I. Mikhailov, “Direct and initiated halogenation of carbon nanomaterials at low temperatures,” *High Energy Chemistry*, vol. 42, no. 4, pp. 311–318, 2008.
- [7] A. Diacon, E. Rusen, B. Mărculescu et al., “Superficial grafting of water-soluble polymers on brominated mwcnt by atrp technique,” *International Journal of Polymer Analysis and Characterization*, vol. 16, no. 1, pp. 1–8, 2011.
- [8] G. Fanchini, H. E. Unalan, and M. Chhowalla, “Modification of transparent and conducting single wall carbon nanotube thin films via bromine functionalization,” *Applied Physics Letters*, vol. 90, no. 9, Article ID 092114, 2007.
- [9] Y. K. Chen, M. L. H. Green, J. L. Griffin, J. Hammer, R. M. Logo, and S. C. Tsang, “Purification and opening of carbon nanotubes via bromination,” *Advanced Materials*, vol. 8, no. 12, pp. 1012–1015, 1996.
- [10] J. Li, L. Vaisman, G. Marom, and J. K. Kim, “Br treated graphite nanoplatelets for improved electrical conductivity of polymer composites,” *Carbon*, vol. 45, no. 4, pp. 744–750, 2007.
- [11] E. Papirer, R. Lacroix, J. B. Donnet, G. Nanse, and P. Fioux, “XPS Study of the halogenation of carbon black-part 1. Bromination,” *Carbon*, vol. 32, no. 7, pp. 1341–1358, 1994.
- [12] E. Unger, A. Graham, F. Kreupl, M. Liebau, and W. Hoenlein, “Electrochemical functionalization of multi-walled carbon nanotubes for solvation and purification,” *Current Applied Physics*, vol. 2, no. 1, pp. 107–111, 2002.
- [13] V. L. Kuznetsov, K. V. Elumeeva, A. V. Ishchenko et al., “Multi-walled carbon nanotubes with ppm level of impurities,” *Physica Status Solidi B*, vol. 247, no. 11-12, pp. 2695–2699, 2010.
- [14] S. Doniach and M. Sunjic, “Many-electron singularity in X-ray photoemission and X-ray line spectra from metals,” *Journal of Physics C*, vol. 3, no. 2, pp. 285–291, 1970.
- [15] D. A. Shirley, “High-resolution x-ray photoemission spectrum of the valence bands of gold,” *Physical Review B*, vol. 5, no. 12, pp. 4709–4714, 1972.
- [16] C. Fitzwater, *Functionalization of multi-walled carbon nanotubes in epoxy composites*, M.S. thesis, 2010.
- [17] A. I. Romanenko, O. B. Anikeeva, T. I. Buryakov et al., “Influence of surface layer conditions of multiwall carbon nanotubes on their electrophysical properties,” *Diamond and Related Materials*, vol. 19, no. 7–9, pp. 964–967, 2010.
- [18] B. L. Altshuler and A. G. Aronov, “Electron-electron interaction in disordered conductors,” in *Electron-Electron Indisordered Systems*, A. L. Efros and M. Pollak, Eds., North-Holland, 1985.
- [19] Z. R. Ismagilov, A. E. Shalagina, O. Y. Podyacheva et al., “Structure and electrical conductivity of nitrogen-doped carbon nanofibers,” *Carbon*, vol. 47, no. 8, pp. 1922–1929, 2009.

## Research Article

# Synthesis of 1D, 2D, and 3D ZnO Polycrystalline Nanostructures Using the Sol-Gel Method

Yung-Kuan Tseng,<sup>1,2</sup> Ming-Hung Chuang,<sup>2</sup> Yen-Cheng Chen,<sup>2</sup> and Chao-Hsien Wu<sup>2</sup>

<sup>1</sup>Department of Cultural Heritage Conservation, National Yunlin University of Science and Technology, Douliou 64002, Taiwan

<sup>2</sup>Graduate School of Materials Science, National Yunlin University of Science and Technology, Douliou 64002, Taiwan

Correspondence should be addressed to Yung-Kuan Tseng, kuan@yuntech.edu.tw

Received 4 December 2011; Accepted 25 February 2012

Academic Editor: Yahya A. Ismail

Copyright © 2012 Yung-Kuan Tseng et al. This is an open access article distributed under the Creative Commons Attribution License, which permits unrestricted use, distribution, and reproduction in any medium, provided the original work is properly cited.

This study employed various polyol solvents to synthesize zinc oxide polycrystalline nanostructures in the form of fibers (1D), rhombic flakes (2D), and spheres (3D). The synthetic process primarily involved the use of zinc acetate dihydrate in polyol solutions, which were used to derive precursors of zinc alkoxides. Following hydrolysis at 160°C, the zinc alkoxide particles self-assembled into polycrystalline nanostructures with different morphologies. Following calcination at 500°C for 1 h, polycrystalline ZnO with good crystallinity was obtained. FE-SEM explored variations in surface morphology; XRD was used to analyze the crystalline structures and crystallinity of the products, which were confirmed as ZnO wurtzite structures. FE-TEM verified that the ZnO nanostructures were polycrystalline. Furthermore, we employed TGA/DSC to observe the phase transition. According to the results of property analyses, we proposed models of the relevant formation mechanisms. Finally, various ZnO structures were applied in the degradation of methylene blue to compare their photocatalytic efficiency.

## 1. Introduction

In recent years, zinc oxide (ZnO) has become the subject of much research due to its excellent attributes as an II–VI semiconductor [1, 2]. At room temperature, it possesses a wide direct band gap (3.37 eV) as well as a high exciton binding energy of approximately 60 meV [3]. By contrast, the free exciton binding energy of GaN is only 26 meV. Greater exciton binding energy enhances the light emission efficiency of excitons at room temperature [4], the mechanism of which can be applied in photoelectric conversion components, solar cells, UV lasers, piezoelectric and thermoelectric materials, nanometer photocatalysts, and gas sensors. Furthermore, ZnO has high thermal stability and UV absorption but does not absorb visible light, enabling its use in transparent conductive components. As well as titanium dioxide, ZnO is also an effective photocatalyst.

The application of ZnO nanostructures in nanodevices has attracted considerable attention in the last few years, leading to studies on various forms of syntheses. For example, many studies have conducted cylindrical, linear,

and tubular forms of one-dimensional syntheses [5–9]; research on two-dimensional nanostructures is relatively rare [10–13]; more complex three-dimensional nanostructures are composed of low-dimensional nanostructures [14, 15].

Currently, there are many methods to fabricate ZnO nanostructures or microstructures. Oxidation of zinc vapor [16] involves placing metal zinc powder into a crucible and heating it in a furnace; at 419.53°C, the powder melts into liquid state before evaporating into zinc vapor. Oxygen is introduced to react with the zinc vapor and form needle-shaped crystal whiskers of ZnO. Chemical vapor deposition (CVD) [17] is another approach that utilizes energy sources such as heat, plasma discharge, or UV irradiation to enable chemical reactions of vapor substances on the heated surface of a solid, where the stable solid products of the reaction are deposited. The vapor-liquid-solid method (VLS) [18, 19] is the most common process for the fabrication of ZnO nanostructures. High temperatures are required to vaporize or decompose ZnO growth sources; a catalyst and the resulting zinc vapor then produce an alloy with a low melting point. Zinc precipitates from the supersaturated

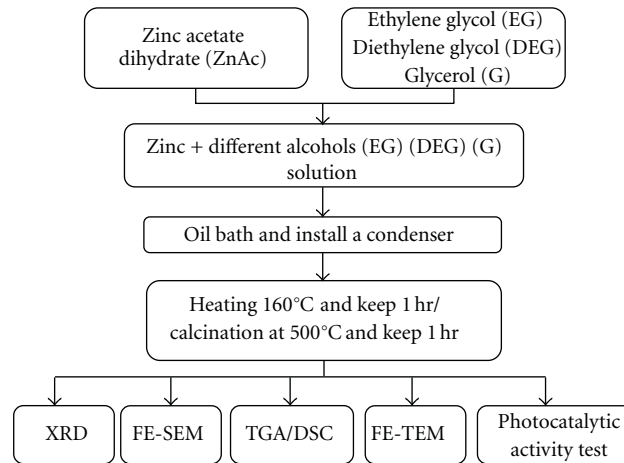


FIGURE 1: Procedure of the experiment.

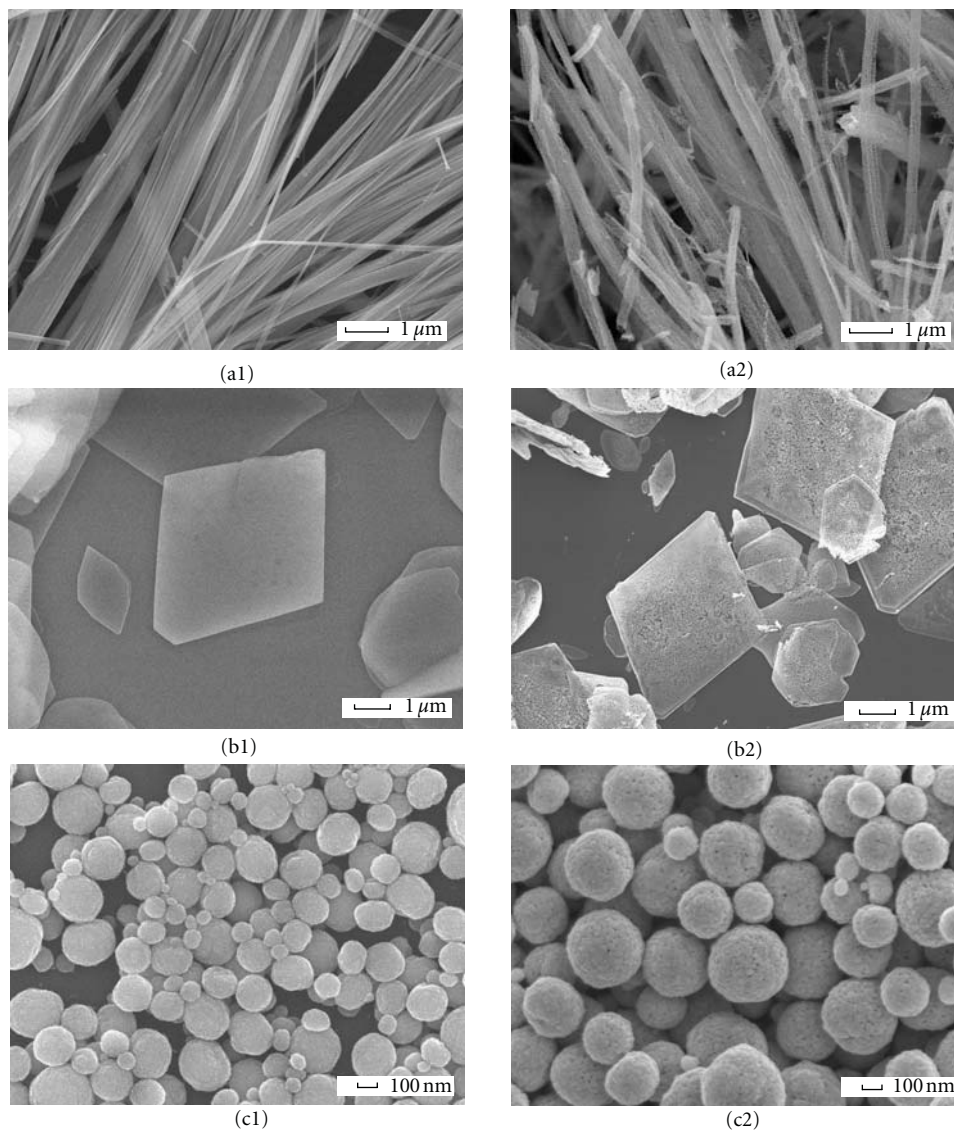


FIGURE 2: Various surface morphologies of synthesized ZnO: (a1), (b1), and (c1) ZnO gel solutions dried at 160°C; (a2), (b2), and (c2) samples calcinated at 500°C.

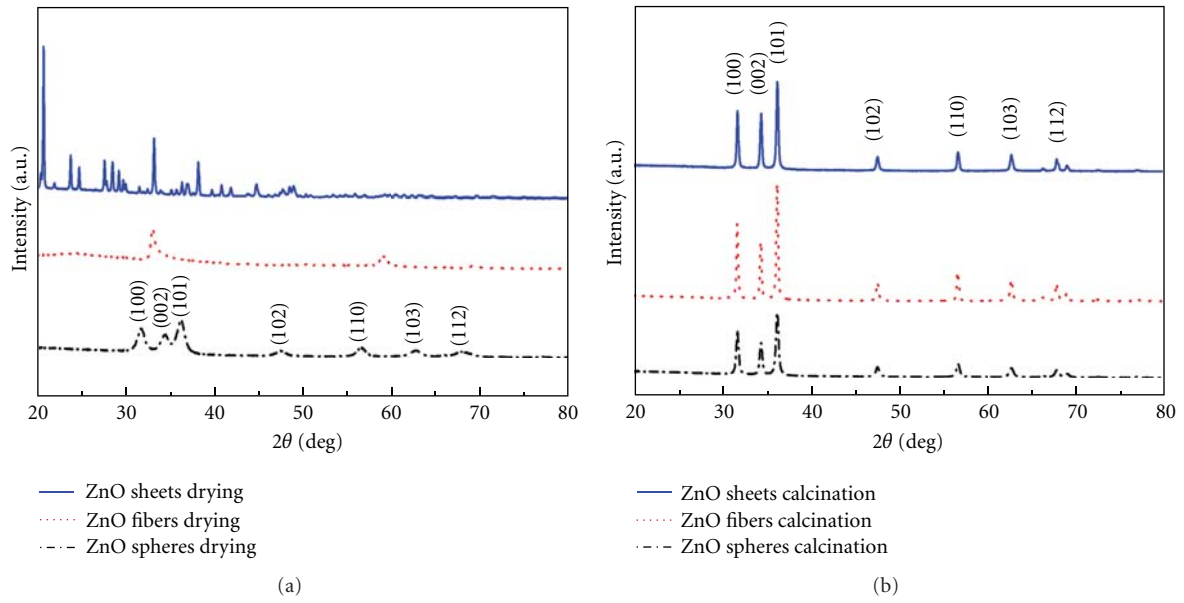


FIGURE 3: XRD graphs of ZnO fibers, ZnO spheres, and ZnO flakes following (a) drying at 160°C and (b) calcination at 500°C.

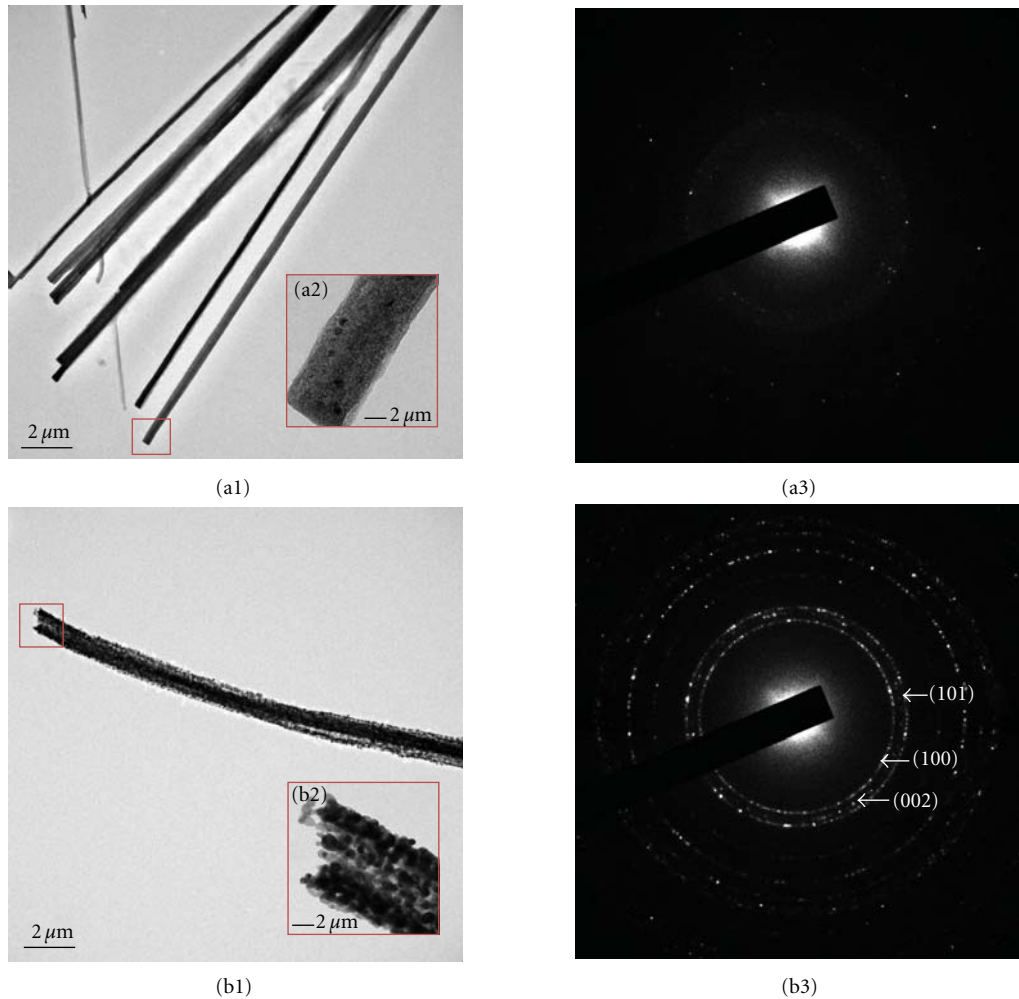


FIGURE 4: SAED graphs and FE-TEM images of ZnO fibers: (a1), (a2), and (a3) samples dried at 160°C; (b1), (b2), and (b3) samples calcinated at 500°C.

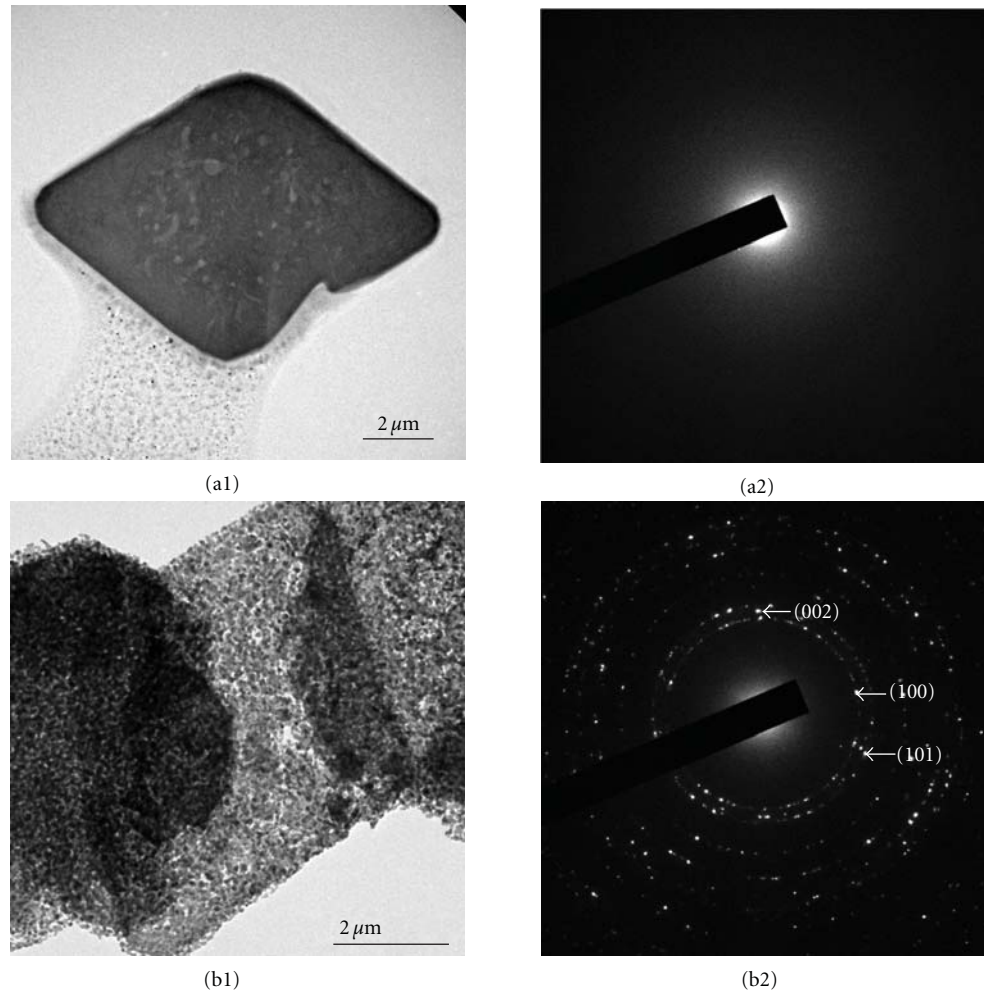


FIGURE 5: SAED graphs and FE-TEM images of ZnO flakes: (a1) and (a2) samples dried at 160°C; (b1) and (b2) samples calcinated at 500°C.

alloy before merging with atmospheric oxygen to form ZnO nanowires. The ZnO nanowires synthesized via the VLS method are generally monocrystalline, the diameter of which is determined by the particle size of the catalyst. Finally, the template-based method [20] employs methods such as electroplating, CVD, and the sol-gel method to grow the desired substance in the holes of a porous alumina substrate, the growth template. The ZnO nanostructures obtained from this method are polycrystalline.

Regardless of monocrystalline or polycrystalline results, most methods for producing ZnO structures require high temperatures or high costs. This study proposes a low-cost sol-gel method to fabricate various forms of ZnO structures. This novel process is fast and can be completed at lower temperatures. Moreover, the photocatalytic effect of the fiber ZnO structures produced with ethylene glycol as the solvent is superior to that of commercial ZnO.

## 2. Experiment Methods

*2.1. Synthesis.* All of the chemicals employed in this study were of analytical grade and required no further purification.

This study employed three alcohols as solvents in the sol-gel method to fabricate various ZnO nanostructures: ethylene glycol (EG), glycerol (G), and diethylene glycol (DEG). The structural, physical, and optical properties of the ZnO products generated from the three solvents were compared.

The synthesis was divided into three processes: solution preparation, heating to promote hydrolysis, and heat treatment of the products.

The steps involved in the synthesis are as follows.

- (1) 0.1 M of zinc acetate dihydrate ( $\text{Zn}(\text{CH}_3\text{COO})_2 \cdot 2\text{H}_2\text{O}$ ) is placed in a 250 mL round-bottom flask.
- (2) 100 mL of the solvent (EG, G, or DEG) is added to the flask.
- (3) The round-bottom flask is equipped with a reflux apparatus and placed in an oil bath, where the solution is heated and stirred.
- (4) The solution is heated at a rate of 1°C/min. When the temperature approaches 160°C, the clear solution becomes milky white. The temperature of the solution is maintained at 160°C for 1 h.

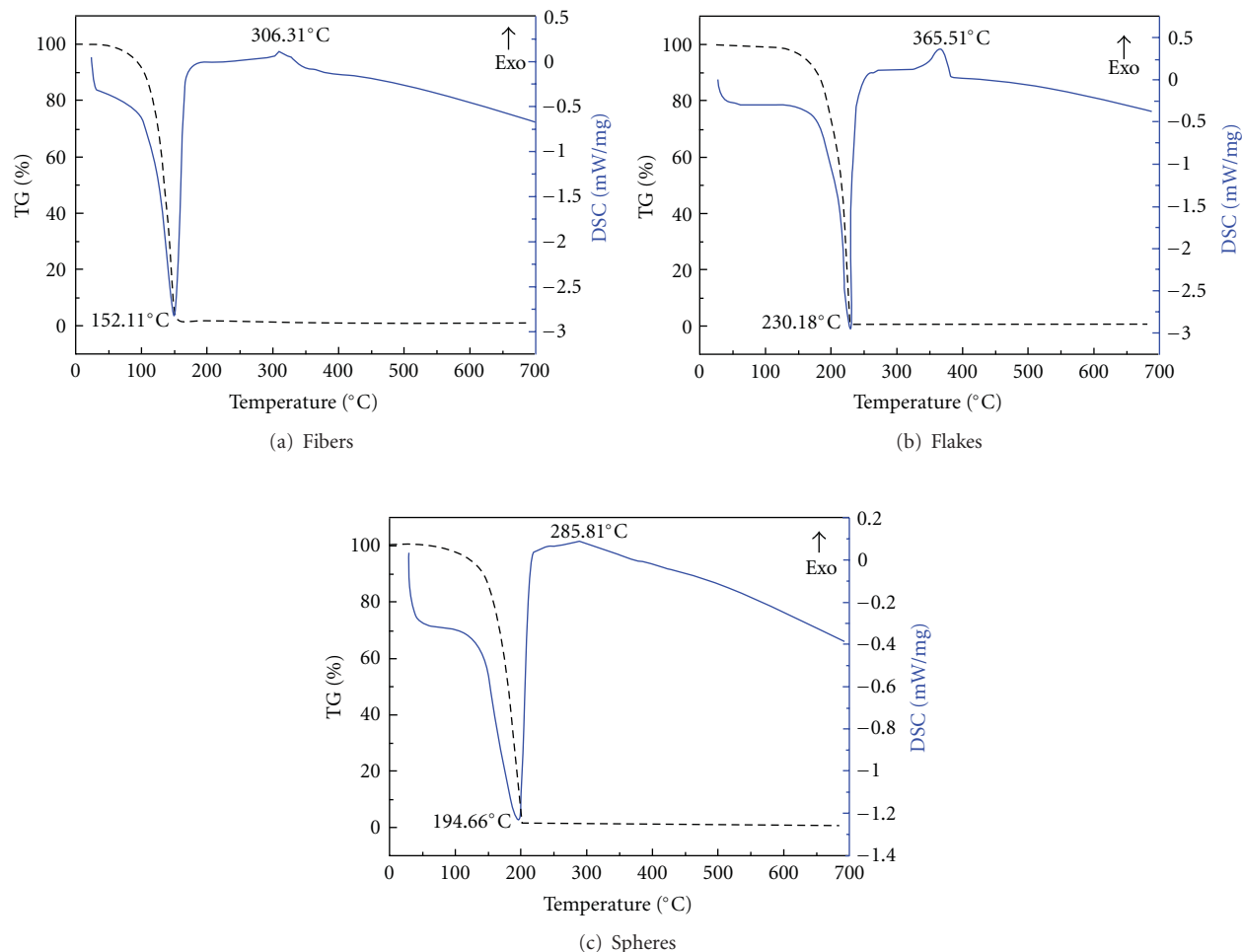


FIGURE 6: TGA/DSC graphs of the precursor of various ZnO structures: (a) fibers, (b) flakes, and (c) spheres.

(5) The milky white solution is dripped onto silicon substrates and dried on a hot plate at  $160^{\circ}\text{C}$ , forming one sample type. For the other sample type, the solution is placed in a high-temperature furnace and heated to  $500^{\circ}\text{C}$  at a rate of  $5^{\circ}\text{C}/\text{min}$  under atmospheric conditions. The temperature is maintained for 1 h, and the sample is taken out once its temperature cools to room temperature.

The experimental procedure is illustrated in Figure 1.

**2.2. Property Analysis.** Field emission scanning electron microscopy (FE-SEM, JEOL JSM7500F) was performed on the sample dried at  $160^{\circ}\text{C}$  and the sample calcinated at  $500^{\circ}\text{C}$  to explore their surface morphology. High-resolution X-ray diffraction (HR-XRD, PHILIPS X'PERT Pro MPD) was employed to analyze the structural properties of the samples, and the phase transition during the synthetic process was observed using simultaneous thermogravimetric analyzer and differential scanning calorimeter (TGA/DSC, TA Instruments-SDT 2960). A field emission transmission electron microscope (FE-TEM JEOL JEM-2100F) was used to observe the appearance and crystalline structure.

**2.3. Photocatalytic Activity Test.** Three different morphologies of synthesized ZnO were compared with commercial ZnO. Samples were placed in methylene blue solutions and exposed to UV-C light for an hour. The absorption values of the samples were measured every 20 min using UV-visible spectroscopy (JASCO V-630).

### 3. Results and Discussion

**3.1. Surface Morphology.** From FE-SEM observations, this study determined that the application of zinc acetate dihydrate as a solute in conjunction with EG, G, and DEG as solvents in sol-gel reactions enables the formation of ZnO with varying morphologies. Figure 2 presents the various types of ZnO that can be obtained from ZnAc with various polyols and heat treatments. Using EG, G, and DEG as the solvents resulted in fiber structures (Figures 2(a1) and 2(a2)), flake structures (Figures 2(b1) and 2(b2)), and spherical structures (Figures 2(c1) and 2(c2)), respectively. All of the samples with gel solutions synthesized at  $160^{\circ}\text{C}$  and then dried on a hot plate at  $160^{\circ}\text{C}$  presented a smooth micro-morphology (Figures 2(a1), 2(b1), and 2(c1)). The samples

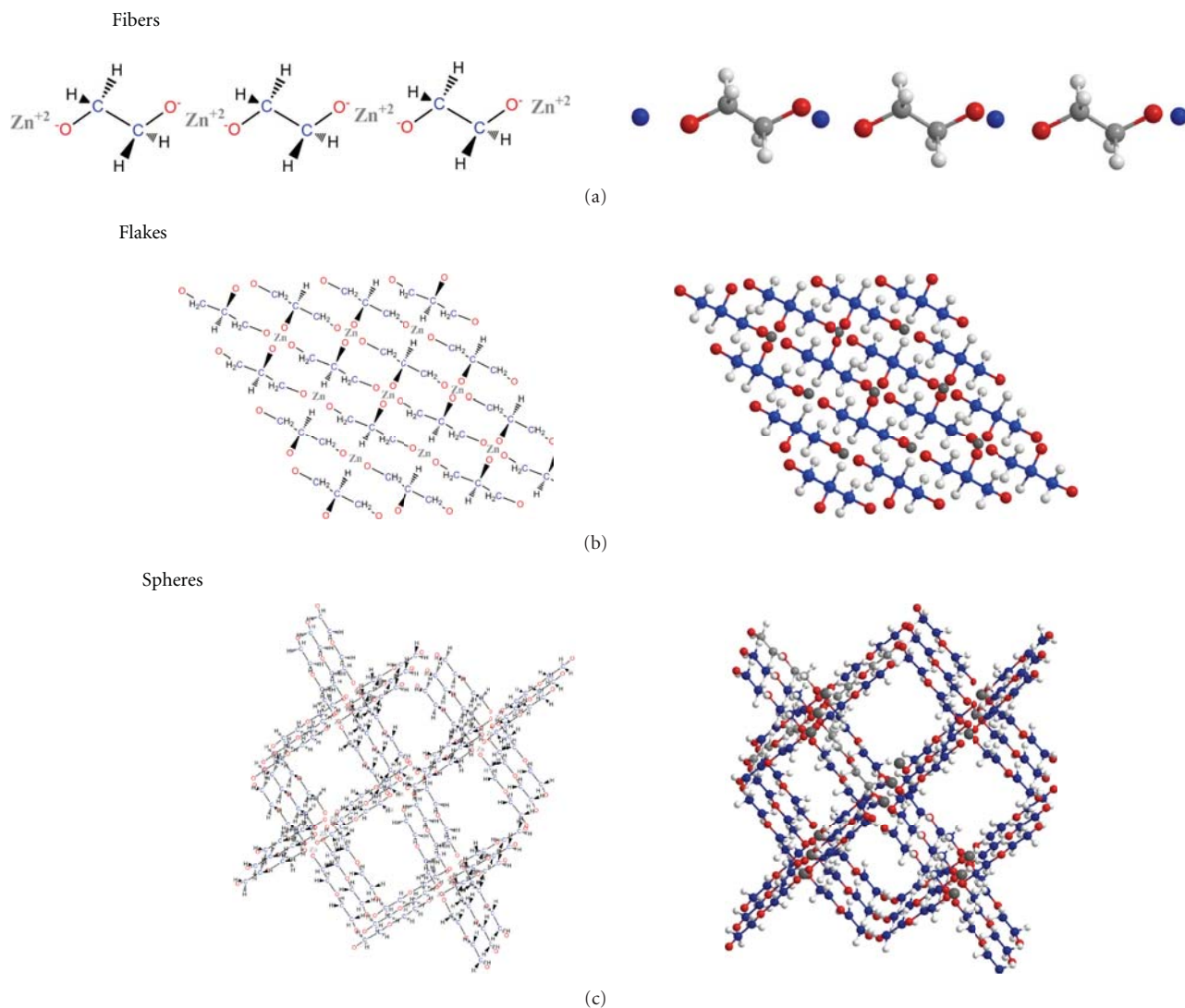


FIGURE 7: Formation mechanisms of ZnO fibers (1D), ZnO flakes (2D), and ZnO spheres (3D). Color code: blue: carbon, white: hydrogen, red: oxygen, and grey: zinc.

calcinated in air at 500°C remained unchanged in shape but exhibited rougher surfaces with additional holes and cracks (Figures 2(a2), 2(b2), and 2(c2)), which were due to the conversion of the larger zinc alkoxide particles into the smaller ZnO crystals.

**3.2. Structural Properties.** Figure 3 shows the XRD graphs of the three types of zinc compound dried at 160°C and calcinated at 500°C. The graphs of the samples dried at 160°C were compared with JCPDS files, of which no files were found to be identical to the ZnO flakes and fibers. No similar graphs were found in the literature either. We speculate that the two XRD graphs are consistent with the crystal structure of zinc alkoxides. The spherical structures dried at 160°C are consistent with ZnO structures, as shown in Figure 3(a). This indicates that using DEG as the solvent can hydrolyze ZnAc into ZnO at lower temperatures. Regarding the three samples calcinated at 500°C, the XRD

graphs were recognized as identical to nos. 36-1451 in the JCPDS files, namely, wurtzite structures (Figure 3(b)).

Figure 4 shows the appearance and crystalline structure of the zinc compounds observed by FE-TEM. Figure 4(a1) shows the ZnO fibers synthesized at 160°C; Figure 4(a2) is a partial enlargement of Figure 4(a1). Figure 4(a3) is the selected area electron diffraction (SAED) graph of the ZnO fibers; some crystals, speculated as ZnO fiber structures, are already apparent. Figure 4(b1) is an image of the ZnO fibers calcinated at 500°C; Figure 4(b2) is a partial enlargement of Figure 4(b1). Figure 4(b3) exhibits the SAED graph following calcinations, revealing superior crystallinity to that in Figure 4(a3). Figures 5(a1) and 5(a2) are the SAED graphs of the ZnO flakes synthesized at 160°C, and Figures 5(b1) and 5(b2) are the SAED graphs of the calcinated ZnO flakes. Figures 4 and 5 demonstrate that the number of holes and cracks increases when zinc alkoxide turns into ZnO during calcination. Moreover, the crystallinity improves, and

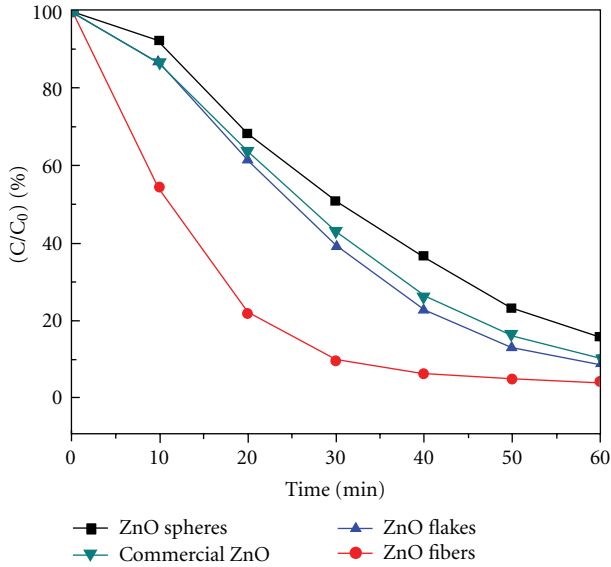


FIGURE 8: Comparison of photocatalytic effects of various ZnO structures.

polycrystalline structures form, which correspond with the XDR graphs.

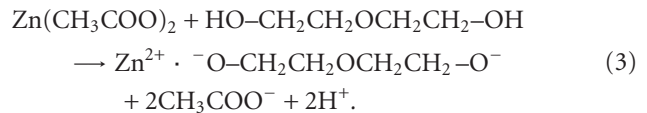
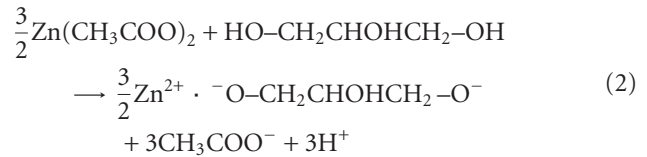
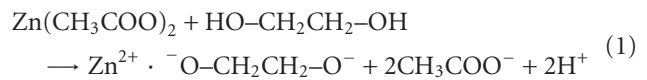
The precursor solutions of the three different morphologies of ZnO were further analyzed by TGA/DSC to investigate the influence of the heat treatment on the samples. Figure 6 presents the results of the TGA/DSC analysis. Each sample exhibited a distinct endothermic peak followed by a marked loss in weight at the lower temperatures of 152.11°C, 230.18°C, and 194.66°C, respectively. The endothermic peaks and weight loss are primarily caused by the vaporization of the alcohols in the solution, leaving zinc alkoxide behind. Furthermore, the three different surface morphologies of ZnO showed exothermic peaks at 306.31°C, 365.51°C, and 285.81°C, respectively, indicating the pyrolysis of zinc alkoxide and the energy required for it to sinter into ZnO. As seen in Figure 6, spherical structures require the least amount of energy to be converted into ZnO, thereby explaining the reason why the spherical sample is capable of forming crystalline ZnO structures at a lower temperature.

**3.3. Formation Mechanism.** Due to the heating, the ZnAc within the solution undergoes hydrolysis forming acetate ions and zinc ions. With the abundance of electrons in the oxygen atoms, the hydroxyl groups (–OH) of alcohol molecules bond with the zinc ions. The resulting alkoxides are such as shown in (1)–(3). Figure 7 presents the bonding processes for ZnO fiber structures, sheet structures, and spherical structures. When using EG as the solvent, the two sides of the zinc ions form ionic bonds with the oxygen ions, which link to more ions and form long fiber-like structures (Figure 7(a)).

With G as the solvent, the glycerol possesses three hydroxyl groups that can react with the zinc ions. Because the electronic configuration of the zinc ions is [Ar]3d<sup>10</sup>, 4s and 4p merge into an empty sp<sup>3</sup> orbital, which further

forms coordinate covalent bonds with the oxygen ions in the alkoxy groups created by the glycerol. Under the conditions enabling the formation of coordinate covalent bonds with minimal three-dimensional obstacles, simulation showed the resulting sheet structures exhibited in (Figure 7(b)).

The reaction principles under the circumstances with DEG as the solvent are similar to those with glycerol. Due to the longer molecular structures of DEG and in consideration of conditions enabling the formation of coordinate covalent bonds with minimal three-dimensional obstacles, 3D structures are more probable (Figure 7(c)). These 3D structures form sphere colloid particles, which further cluster into larger spherical structures. As observed in microscopic images shown in Figure 2, the spherical structures are in fact clusters of smaller spherical structures:



**3.4. Photocatalytic Activity Test.** 4 mL of 5 ppm methylene blue solution was respectively added to 0.1 g of the three types of ZnO and commercial ZnO, followed by irradiation with 254 nm UV light. The degradation rate of ZnO fibers as the catalyst was the highest (Figure 8); after 10 minutes, the concentration of methylene blue reduced by 50%. The concentrations of the methylene blue solutions added to the ZnO sheets, ZnO spheres, and commercial ZnO were still approximately 90%. The degradation rates from the highest to the lowest were ZnO fibers > ZnO sheets > commercial ZnO > ZnO spheres.

## 4. Conclusion

This study employed the sol-gel method to synthesize ZnO polycrystalline nanostructures using ZnAc as the solute and various polyols as solvents (EG, G, and DEG). Zinc alkoxide crystals of varying morphologies were successfully fabricated at 160°C. The EG, G, and DEG solvents synthesized fiber-like nanostructures, rhombic flakes, and spherical particles, respectively. The surface morphology of the samples dried at 160°C was smooth. By contrast, the samples calcinated at 500°C in air gained sufficient energy to enable pyrolysis of the zinc alkoxide and sintering into the smaller ZnO molecules. Consequently, a considerable number of cracks and holes appeared, which, however, had no effect on the overall morphology. The XRD graphs and FE-TEM images mutually verify the increase in crystallinity following calcination as well as the polycrystalline structures of ZnO.

By the results, we proposed models of the relevant formation mechanisms taking into account ionic bonding and three-dimensional obstacles. A photocatalyst activity test was performed on the synthetic products and the commercial ZnO. The results indicate that the catalytic effect of ZnO fibers was the most effective.

## References

- [1] D. C. Look, J. W. Hemsky, and J. R. Sizelove, "Residual native shallow donor in ZnO," *Physical Review Letters*, vol. 82, no. 12, pp. 2552–2555, 1999.
- [2] Y. W. Heo, D. P. Norton, L. C. Tien et al., "ZnO nanowire growth and devices," *Materials Science and Engineering R*, vol. 47, no. 1-2, pp. 1–47, 2004.
- [3] K. Ellmer, "Resistivity of polycrystalline zinc oxide films: current status and physical limit," *Journal of Physics D*, vol. 34, no. 21, pp. 3097–3108, 2001.
- [4] A. Ohtomo, M. Kawasaki, Y. Sakurai et al., "Fabrication of alloys and superlattices based on ZnO towards ultraviolet laser," *Materials Science and Engineering B*, vol. 56, no. 2-3, pp. 263–266, 1998.
- [5] J. Wang and L. Gao, "Synthesis and characterization of ZnO nanoparticles assembled in one-dimensional order," *Inorganic Chemistry Communications*, vol. 6, no. 7, pp. 877–881, 2003.
- [6] A. Kajbafvala, M. R. Shayegh, M. Mazloumi et al., "Nanostructure sword-like ZnO wires: rapid synthesis and characterization through a microwave-assisted route," *Journal of Alloys and Compounds*, vol. 469, no. 1-2, pp. 293–297, 2009.
- [7] P. Li, Y. Wei, H. Liu, and X. Wang, "A simple low-temperature growth of ZnO nanowhiskers directly from aqueous solution containing  $\text{Zn}(\text{OH})_4^{2-}$  ions," *Chemical Communications*, no. 24, pp. 2856–2857, 2004.
- [8] S. W. Kuo, Y. C. Chung, K. U. Jeong, and F. C. Chang, "A simple route from monomeric nanofibers to zinc oxide/zinc sulfide nanoparticle/ polymer composites through the combined use of  $\gamma$ -irradiation polymerization, gas/solid reaction and thermal decomposition," *Journal of Physical Chemistry C*, vol. 112, no. 42, pp. 16470–16477, 2008.
- [9] C. Bae, H. Yoo, S. Kim et al., "Template-directed synthesis of oxide nanotubes: fabrication, characterization, and applications," *Chemistry of Materials*, vol. 20, no. 3, pp. 756–767, 2008.
- [10] Q. Cui, K. Yu, N. Zhang, and Z. Zhu, "Porous ZnO nanobelts evolved from layered basic zinc acetate nanobelts," *Applied Surface Science*, vol. 254, no. 11, pp. 3517–3521, 2008.
- [11] L. Wu, Y. Wu, and Y. Lü, "Self-assembly of small ZnO nanoparticles toward flake-like single crystals," *Materials Research Bulletin*, vol. 41, no. 1, pp. 128–133, 2006.
- [12] S. -H. Yu and M. Yoshimura, "Shape and phase control of ZnS nanocrystals: template fabrication of wurtzite ZnS single-crystal nanosheets and ZnO flake-like dendrites from a lamellar molecular precursor  $\text{ZnS} \cdot (\text{NH}_2 \text{CH}_2 \text{CH}_2 \text{NH}_2)_{0.5}$ ," *Advanced Materials*, vol. 14, no. 4, pp. 296–300, 2002.
- [13] S. Chen, Y. Liu, C. Shao et al., "Structural and optical properties of uniform ZnO nanosheets," *Advanced Materials*, vol. 17, no. 5, pp. 586–590, 2005.
- [14] L. Tang, S. Yang, Y. Guo, and B. Zhou, "Building block-tunable synthesis of self-assembled ZnO quasi-microspheres via a facile liquid process," *Chemical Engineering Journal*, vol. 165, no. 1, pp. 370–377, 2010.
- [15] H. Wang, K. P. Yan, J. Xie, and M. Duan, "Fabrication of ZnO colloidal photonic crystal by spin-coating method," *Materials Science in Semiconductor Processing*, vol. 11, no. 2, pp. 44–47, 2008.
- [16] W. Lee, M. C. Jeong, and J. M. Myoung, "Catalyst-free growth of ZnO nanowires by metal-organic chemical vapour deposition (MOCVD) and thermal evaporation," *Acta Materialia*, vol. 52, no. 13, pp. 3949–3957, 2004.
- [17] B. P. Zhang, N. T. Binh, K. Wakatsuki et al., "Pressure-dependent ZnO nanocrystal growth in a chemical vapor deposition process," *Journal of Physical Chemistry B*, vol. 108, no. 30, pp. 10899–10902, 2004.
- [18] Y. W. Wang, L. D. Zhang, G. Z. Wang, X. S. Peng, Z. Q. Chu, and C. H. Liang, "Catalytic growth of semiconducting zinc oxide nanowires and their photoluminescence properties," *Journal of Crystal Growth*, vol. 234, no. 1, pp. 171–175, 2002.
- [19] M. H. Huang, Y. Wu, H. Feick, N. Tran, E. Weber, and P. Yang, "Catalytic growth of zinc oxide nanowires by vapor transport," *Advanced Materials*, vol. 13, no. 2, pp. 113–116, 2001.
- [20] C. H. Liu, W. C. Yiu, F. C. K. Au, J. X. Ding, C. S. Lee, and S. T. Lee, "Electrical properties of zinc oxide nanowires and intramolecular p-n junctions," *Applied Physics Letters*, vol. 83, no. 15, pp. 3168–3170, 2003.

## Research Article

# Interconnected TiO<sub>2</sub> Nanowire Networks for PbS Quantum Dot Solar Cell Applications

Fan Xu,<sup>1</sup> Jaime Benavides,<sup>1</sup> Xin Ma,<sup>1</sup> and Sylvain G. Cloutier<sup>1,2</sup>

<sup>1</sup>Department of Electrical and Computer Engineering, University of Delaware, 140 Evans Hall, Newark, DE 19716, USA

<sup>2</sup>Département de Génie Électrique, École de Technologie Supérieure, 1100 rue Notre-Dame Ouest, Montréal, QC, Canada H3C1K3

Correspondence should be addressed to Sylvain G. Cloutier, sylvain.g.cloutier@etsmtl.ca

Received 21 November 2011; Revised 7 February 2012; Accepted 15 February 2012

Academic Editor: Sharad D. Bhagat

Copyright © 2012 Fan Xu et al. This is an open access article distributed under the Creative Commons Attribution License, which permits unrestricted use, distribution, and reproduction in any medium, provided the original work is properly cited.

We present a simple method for the fabrication of an interconnected porous TiO<sub>2</sub> nanostructured film via dip coating in a colloidal suspension of ultrathin TiO<sub>2</sub> nanowires followed by high-temperature annealing. The spheroidization of the nanowires and the fusing of the loosely packed nanowire films at the contact points lead to the formation of nanopores. Using this interconnected TiO<sub>2</sub> nanowire network for electron transport, a PbS/TiO<sub>2</sub> heterojunction solar cell with a large short-circuit current of 2.5 mA/cm<sup>2</sup>, a Voc of 0.6 V, and a power conversion efficiency of 5.4% is achieved under 8.5 mW/cm<sup>2</sup> white light illumination. Compared to conventional planar TiO<sub>2</sub> film structures, these results suggest superior electron transport properties while still providing the large interfacial area between PbS quantum dots and TiO<sub>2</sub> required for efficient exciton dissociation.

## 1. Introduction

Lead chalcogenide colloidal semiconductor nanocrystals can be promising materials for low-cost, large-area, and efficient photovoltaic devices, due to a large Bohr radius, size-effect tunable bandgap across the near-infrared region and large absorption cross-section, as well as the solution processability [1–7]. Over the last few years, Schottky solar cells based on PbS, PbSe, or PbS<sub>x</sub>Se<sub>1-x</sub> quantum dots with power converting efficiency over 3% have been demonstrated [3, 5, 7]. More recently, the depleted-heterojunction quantum dot solar cells based on the PbS/TiO<sub>2</sub> nanocrystals have achieved an unprecedented efficiency of 5.1% [1], and PbS/ZnO photovoltaic devices have exhibited excellent air stability for 1000 h of continuous illumination under ambient atmosphere [2].

In general, the power conversion efficiency of the QDs solar cells is primarily determined by three factors: exciton generation, exciton dissociation, and carrier collection efficiencies. Indeed, it was shown previously that the structure and morphology of the TiO<sub>2</sub> layer can play the key role in achieving efficient extraction and transport of minority carriers in dye- and QDs-sensitized solar cells [8]. The TiO<sub>2</sub> layer requires large surface areas for quantum dots attaching,

as well as rapid electron transport across the film to ensure efficient electron collection by the conductive substrate. The widely used mesoporous TiO<sub>2</sub> nanostructured films can be employed to significantly increase the contact area between TiO<sub>2</sub> and the active quantum dot layer, thus facilitating exciton dissociation before radiative recombination and allowing efficient carrier collection. However, the electronic transport suffers from slow electron diffusion rates and low electron mobility in the structurally disordered TiO<sub>2</sub> mesoporous films [8, 9].

Fabrication of TiO<sub>2</sub> films from one-dimensional nanowire and nanotube structures has proven to be an effective way to improve the overall efficiencies of the devices [9–12]. The one-dimensional nanostructure allows diffusion free electron transport along the axial direction to improve electron collection, while the light scattering effect from the subwavelength features can enhance the effective absorption thickness of the quantum dots layer. Nevertheless, one major concern with lateral nanowires is the smaller surface areas it presents for dye and quantum dot sensitization [8].

In this paper, we report the fabrication of superior TiO<sub>2</sub> film structures for QD solar cells formed by dip coating and annealing of ultrathin TiO<sub>2</sub> nanowire films. This interconnected nanowire network structure maintains the large

surface-to-volume ratio from traditional porous TiO<sub>2</sub> films, while allowing efficient electron transport along the nanowires. As we show, the electron transport and carrier extraction in the TiO<sub>2</sub>/PbS heterojunction solar cell can be significantly improved using this porous interconnected TiO<sub>2</sub> nanowire network film. A superb low-cost solar cell was fabricated with a large short-circuit current of 2.5 mA/cm<sup>2</sup>, a V<sub>oc</sub> of 0.6 V, and a power conversion efficiency of 5.4% achieved under 8.5 mW/cm<sup>2</sup> illumination.

## 2. Experiments

**2.1. Chemicals.** Titanium (IV) butoxide 99% (TBT, Aldrich), oleic acid (90%, Aldrich), titanium (IV) isopropoxide (TTIP, Aldrich, 99.999%), poly(acrylic acid) (M 450,000, Aldrich), ethyl acetate (Aldrich, Anhydrous 99.8%) (EAcAc), ethanol (ACS reagent, ≥99.5% (200 proof, absolute), 1-octadecene (90%, Aldrich), lead oxide (99.99%, Aldrich), hexamethyldisilathiane (Fluka) are used.

**Preparation of TiO<sub>2</sub> Sol-Gel [13].** PAA (0.035 g) and EAcAc (1.7998 g) were mixed and sonicated at room temperature for 5 minutes. Ethyl alcohol (42.3429 g) was added and left reposed for 20 minutes. Finally, TBT (13.7489 g) was added to the mixture and was reposed for another 20 minutes, and distilled water (0.5457 g) was added to start the reaction. The solution was continuously stirred for 8 hours and then aged for 24 hours to form the TiO<sub>2</sub> sol-gel.

**Synthesis of TiO<sub>2</sub> Nanowires [14].** The TiO<sub>2</sub> nanowires were synthesized through the nonhydrolytic ester elimination reaction of titanium isopropoxide and oleic acid. TTIP (3.5 mL) was added to 10 g of OA at room temperature under nitrogen atmosphere. The resulting mixture was heated to 280°C for a period of 20 min and was kept at this temperature for 2 h. The light-yellow solution gradually turned dark brown and then white. The solution was then cooled down to room temperature, excess acetone was added, and the solution was centrifuged to precipitate the nanowires.

**PbS Quantum Dot Synthesis [15].** Lead oxide (0.45 g), octadecene (10 g), and oleic acid (1.34 g) are added to a three-neck flask. The mixture is then heated and kept at 80°C for two hours under vigorous stirring in vacuum to degas the solution and dissolve the mixture. Then, the temperature is kept at 110°C under nitrogen flow for 30 min. Subsequently, a solution made of 210 μL of hexamethyldisilathiane diluted in 4 mL of octadecene is quickly injected into the reaction flask under vigorously stirring. The heating was immediately removed and the reaction solution was allowed to cool down slowly to room temperature. Finally, the colloidal PbS quantum dots are collected by quick injection of the reaction solution into excess amount of acetone (with ratio ~1 : 4) for centrifugation. The precipitates are dried in vacuum and redispersed in hexane. To ensure adequate removal of the reaction solvents, precipitation and redispersion are repeated. The quantum dot solution is filtered with 0.2 μm polytetrafluoroethylene filters before device fabrication.

**Fabrication of Solar Cells.** The ITO glass was cleaned using a sequence of ultrasonic baths of deionized water, acetone and isopropanol. Then, the substrate was dipcoated into the TiO<sub>2</sub> sol-gel for 10 seconds and then withdrawn at 200 mm/min to form a thin layer of planar TiO<sub>2</sub> layer (~35 nm), in order to prevent any shorting of the device. This sol-gel TiO<sub>2</sub> layer was annealed at 500°C for 1 hour in a tube furnace to improve its crystalline structure and its conductivity. After that, the porous TiO<sub>2</sub> layers were fabricated by dip-coating the substrate (immersed in the nanowire solution for 10 seconds, and then withdrawn at 200 mm/min) into the TiO<sub>2</sub> nanowires solution in hexane (~35 mg/mL), followed by another annealing at 500°C for 1 hour in the furnace. To make the porous TiO<sub>2</sub> layer thicker, another layer of TiO<sub>2</sub> nanowire was dip-coated on top and then annealed. The PbS quantum dots are then deposited using the layer by layer spin-coating method [1]. For each cycle, the PbS quantum dot solution (25 mg/mL in hexane) is spin-coated (2000 rpm) on the substrate, then the diluted ethanedithiol solution in acetonitrile (0.02 M) is subsequently spin-coated on top to crosslink the quantum dot and make the quantum dot indissoluble in the original solution, and finally, hexane was spin-coated on the substrate to rinse the quantum dot solid [16]. For both devices, eight layers of quantum dots are deposited. Finally, gold is thermally evaporated on top as the back contact electrode. The solar cell was measured with devices placed on top of an integrated sphere under 8.5 mW/cm<sup>2</sup>, white light illumination. The integrating sphere is connected to a fiber illuminator, and the light was uniformly coupled out from the top port of the integrate sphere.

## 3. Results and Discussions

As shown in Figure 1(a) the free-standing TiO<sub>2</sub> nanowires are typically 100–200 nm in length and 3–4 nm in diameter. As shown in Figure 1(b), the high-resolution TEM analysis of the TiO<sub>2</sub> nanowires confirms their sound crystalline structure. The FFT shown in the inset of Figure 1(b) indicates the nanowires are TiO<sub>2</sub> anatase, and it was imaged with its [100] direction parallel to the electron beam. Here, the long 18-carbon-atom stabilizing surfactant (oleic acid) plays a crucial role in passivating the nanowires to prevent agglomeration; thus a uniformly and loosely compacted TiO<sub>2</sub> nanowires film can be deposited by dip coating the substrate into the nanowire solution, as shown in Figure 2(a).

The TiO<sub>2</sub> nanowire fuse with each other at the contact point via sintering. On the other hand, the one-dimensional nanowire will reduce the aspect ratio and spheroidize owing to surface energy reduction [17]. When the spheroidization stops at the contact points of the nanowires, the porous structure is formed. Thus, a high-surface-area, interconnected porous TiO<sub>2</sub> nanostructure is fabricated using the facile dip-coating and annealing process, as shown in the SEM image in Figure 2(c). Large quantities of pores are distributed randomly on both the surface and the interior of the TiO<sub>2</sub> nanostructure. A high-resolution secondary electron SEM image in Figure 2(d) clearly resolved the porous structure of the film. The irregularly distributed nanopores

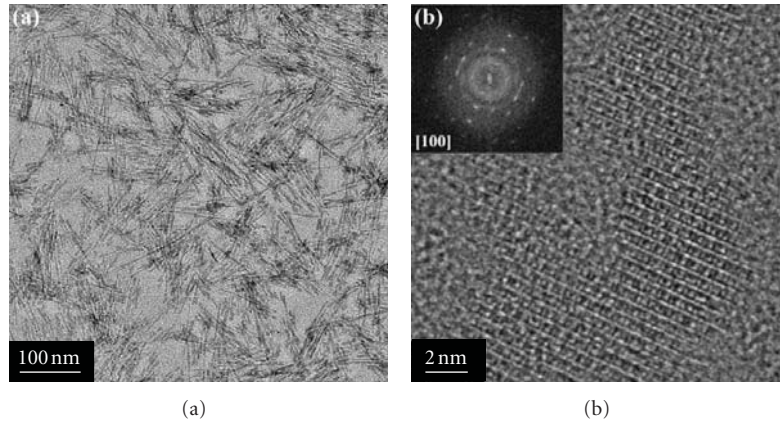


FIGURE 1: (a) Low-resolution TEM image of the free-standing  $\text{TiO}_2$  nanowires after synthesis. (b) The high-resolution TEM image of a single ultrathin  $\text{TiO}_2$  nanowire, the inset shows the corresponding Fast Fourier Transform (FFT) image.

are interconnected by spheroidized NWs after thermal annealing process, with average diameter of  $13.2 \pm 4.7$  nm and average pore area of  $117 \pm 123$  nm<sup>2</sup>. Since the quantum dots used in these devices are typically 3-4 nm in diameter, the relatively larger nanopores can create additional volume for QDs attaching, as well as provide large surface areas to achieve efficient electron extraction.

The SEM image in Figure 3(a) shows the structure of the resulting solar cell device, while the band alignment is shown in Figure 3(b). All the fabrication steps except the evaporation are done in ambient atmosphere. The thickness of the planar  $\text{TiO}_2$  is  $\sim 35$  nm, the porous  $\text{TiO}_2$  nanowire layer is  $\sim 60$  nm, while the PbS quantum-layer is  $\sim 320$  nm.

Figure 4 compares the current density-voltage (J-V) characteristics of a standard PbS quantum dot-sensitized  $\text{TiO}_2$  heterojunction solar cell using a planar  $\text{TiO}_2$  film formed by conventional sol-gel chemistry with the same solar cell using the thick nanoporous interconnected  $\text{TiO}_2$  nanowire network previously deposited on a thin planar  $\text{TiO}_2$  film. Here, small PbS quantum dots of relatively large bandgaps and with their conduction bands well above that of  $\text{TiO}_2$  were used, so as to achieve efficient electronic transfer from the quantum dots to the  $\text{TiO}_2$  [18]. For comparison, both the planar and porous  $\text{TiO}_2$  heterojunction solar cells have equally thick PbS nanocrystalline layers and both were crosslinked using EDT. In contrast with the planar device, the  $\text{TiO}_2$  nanowire device exhibits a superb short-circuit current ( $J_{sc}$ ) of 2.5 mA/cm<sup>2</sup>, a large open-circuit voltage ( $V_{oc}$ ) of 0.6 V, a fill factor of 33%, and a power-converting efficiency of 5.4%. These results suggest that the large surface area in the porous  $\text{TiO}_2$  nanostructured film, as well as an efficient carrier transport along the longitudinal axis of  $\text{TiO}_2$  nanowires, appears to be critical to achieve high  $J_{sc}$  in the heterojunction solar cell architecture. The near-ideal rectifying J-V characteristics of the  $\text{TiO}_2$  nanowire device under dark directly confirm the formation of a high-quality p-n heterojunction between PbS and  $\text{TiO}_2$ . In contrast, the planar  $\text{TiO}_2$  solar cell device suffers from a much smaller short-circuit current ( $J_{sc}$ ), in addition to a significantly lower fill factor of 14%. Moreover, the current drops down rapidly

as the voltage starts to increase. Most likely, this can be attributed to the inefficient electron transport in the planar  $\text{TiO}_2$  layer. Otherwise, it is also possible that pin holes are generated in the planar  $\text{TiO}_2$  film during annealing, thus ruining the performance of the device and explaining the much larger currents observed under forward bias. Since the open-circuit voltage of the devices is mainly determined by difference of the quasi-Fermi level between the PbS nanocrystals and the  $\text{TiO}_2$  layer, both devices exhibit a similar  $V_{oc}$  around 0.6 V.

To better understand the exciton dissociation and electron extraction from the PbS quantum dots to the  $\text{TiO}_2$  we studied the absorption and photoluminescence of EDT-treated nanocrystalline films deposited on glass, planar  $\text{TiO}_2$ , and porous  $\text{TiO}_2$  nanowire network films. Indeed, the electron transfer from small PbS nanocrystals to the  $\text{TiO}_2$  can be monitored through the shift and quenching of the absorption and photoluminescence spectra [19, 20]. The conduction band of the small quantum dots lies well above that of the  $\text{TiO}_2$  thus the high-energy excitons generated upon the absorption of high-energy photons in small QDs can rapidly dissociate with electrons injected to the  $\text{TiO}_2$  layer. The porous  $\text{TiO}_2$  nanowire structure provides large interfacial areas between QDs and  $\text{TiO}_2$ , thus enables efficient electron transfer [21]. This rapid relaxation of high-energy excitons can in turn improve the absorption of high-energy photon by rapid depopulating the excitons in the QDs. As seen in Figure 5(a), the absorption spectrum of the PbS nanocrystals deposited on porous  $\text{TiO}_2$  nanowire structure displays a stronger absorption on the high-energy side and an obviously blue shift compared to the QDs deposited on planar  $\text{TiO}_2$ .

Meanwhile, the photoluminescence of the quantum dots is quenched owing to hot electron transfer to  $\text{TiO}_2$ . Figure 5(b) compares the photoluminescence of monolayer of nanocrystals deposited on glass, on planar  $\text{TiO}_2$  and on the porous  $\text{TiO}_2$ , nanowire network. Due to the photoluminescence quenching at the high energy side, the photoluminescence of the PbS quantum dots exhibits a 24 nm red-shift on planar  $\text{TiO}_2$ , compared with a remarkable 76 nm red shift

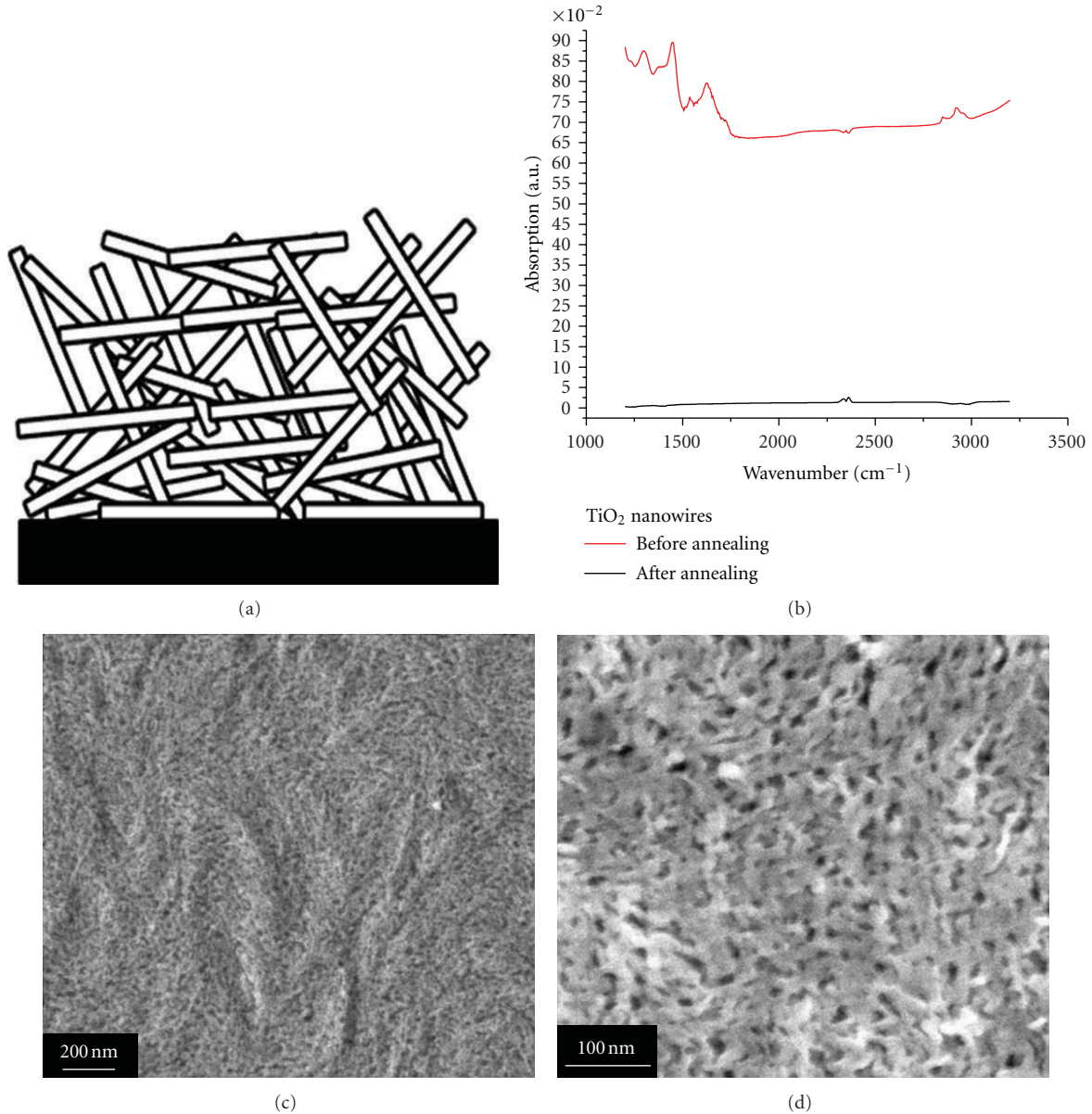


FIGURE 2: (a) A cartoon showing the loosely packed TiO<sub>2</sub> nanowire film fabricated using the dip-coating process. (b) FTIR spectrum of TiO<sub>2</sub> nanowire film dip-coated on a glass slide before and after thermal annealing. (c) SEM image showing the overview of the porous TiO<sub>2</sub> nanostructure. (d) High-resolution second-electron SEM image showing the porous interconnected TiO<sub>2</sub> nanowire network structure after annealing.

on the porous TiO<sub>2</sub> nanowire network film. The strong absorption on the high-energy side combined with the significant quenched and red shifted photoluminescence indicates that efficient electron transfer is achieved between the PbS quantum dots and the porous TiO<sub>2</sub> nanowire. This is also consistent with the superb short-circuit current observed for the porous TiO<sub>2</sub> nanowire-based devices owing to its large interfacial areas and strong electron extraction ability.

#### 4. Conclusions

In summary, we fabricated a high-performance porous TiO<sub>2</sub> film for nanocrystal-sensitized solar cell using an inter-

connected TiO<sub>2</sub> nanowire network. This facile all-solution-based method simply relies on dip coating and annealing of ultrathin TiO<sub>2</sub> nanowires. This unique nanostructured film provides large interfacial area allowing efficient electron extraction from quantum dots and uses the one-dimensional morphology of the TiO<sub>2</sub> nanowires to favor direct electron transport along the long axial direction to improve electron collection. The heterojunction solar cells using this porous interconnected TiO<sub>2</sub> nanowire network films exhibit a superb  $J_{sc}$  of 2.5 mA/cm<sup>2</sup>, a large  $V_{oc}$  of 0.6 V, and a power conversion efficiency of 5.4% under 8.5 mW/cm<sup>2</sup> white-light illumination. Through the absorption and photoluminescence study of the same PbS quantum dots deposited

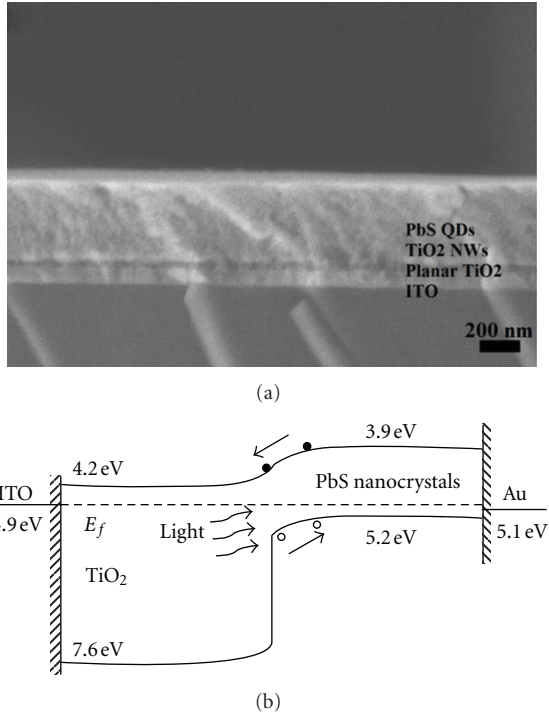


FIGURE 3: (a) SEM image showing the cross-section of the PbS-TiO<sub>2</sub> heterojunction solar cell device. (b) Band diagram of the device.

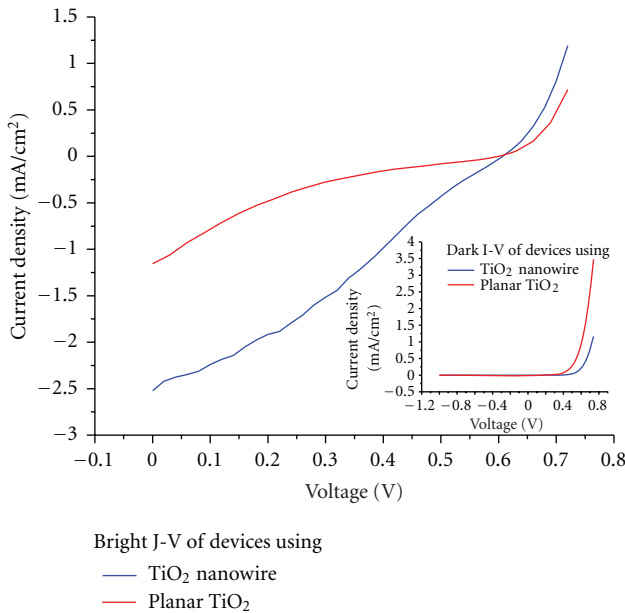


FIGURE 4: Comparison of the current density-voltage (J-V) characteristics under illumination for a standard PbS quantum-dot-sensitized TiO<sub>2</sub> heterojunction solar cell using a planar TiO<sub>2</sub> film formed by conventional sol-gel chemistry with the same solar cell using our thick nanoporous interconnected TiO<sub>2</sub> nanowire network previously deposited on a thin planar TiO<sub>2</sub> film. Both devices are measured under a uniform 8.5 mW/cm<sup>2</sup> white-light illumination. The inset shows the dark I-V characteristics for both devices.

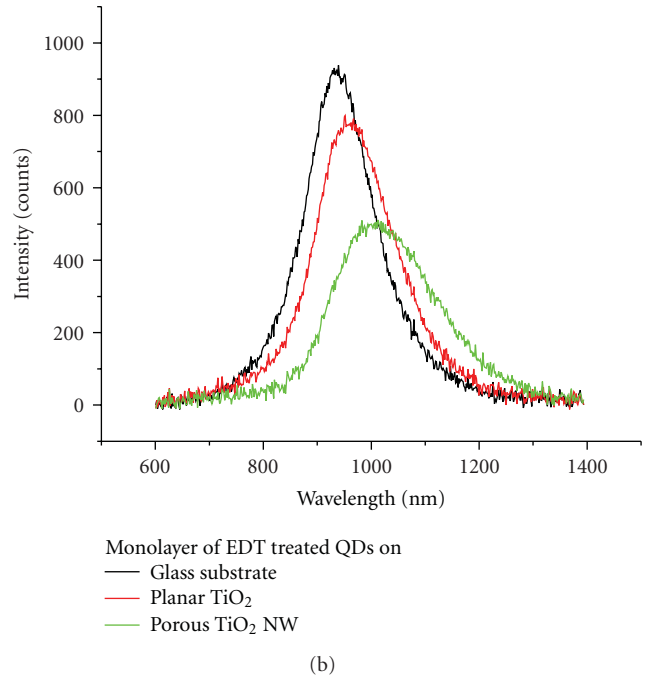
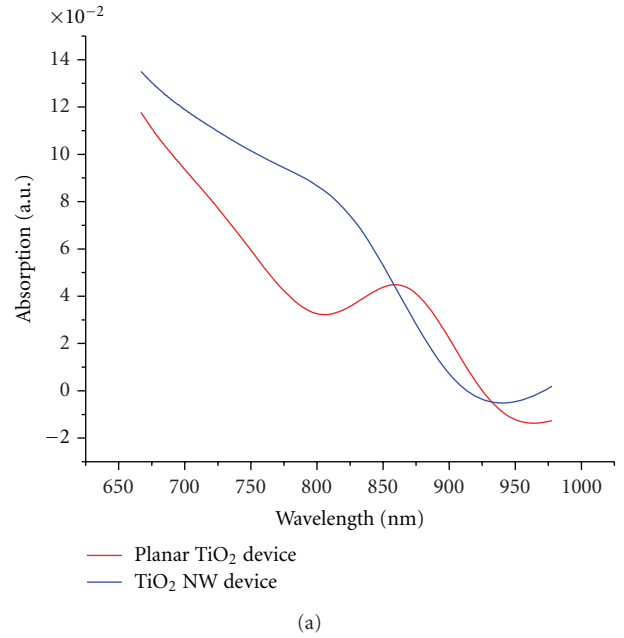


FIGURE 5: (a) Absorption spectrum for the same PbS nanocrystals deposited on planar TiO<sub>2</sub> and porous interconnected TiO<sub>2</sub> nanowire network film. (b) Photoluminescence from a monolayer of the same EDT-treated PbS nanocrystals deposited on glass, on planar TiO<sub>2</sub>, on a porous TiO<sub>2</sub> nanowire network film.

on various TiO<sub>2</sub> substrates, we demonstrated a significantly improved electron-transfer efficiency using the TiO<sub>2</sub> nanowire network structure instead of a conventional planar TiO<sub>2</sub> film structure.

## Acknowledgments

The authors would like to thank Sangcheol Kim for the absorption measurements and Xiaoqian Ma for FTIR measurements. This work was supported through the AFOSR (FA9550-10-1-0363), through the DARPA COMPASS Program via a Grant from the DOI NBC (N11AP20031), the DARPA young Faculty Award Program and the ETS Institutional Research Chair Program to whom we are most thankful.

## References

- [1] A. G. Pattantyus-Abraham, I. J. Kramer, A. R. Barkhouse et al., "Depleted-heterojunction colloidal quantum dot solar cells," *ACS Nano*, vol. 4, no. 6, pp. 3374–3380, 2010.
- [2] J. M. Luther, J. Gao, M. T. Lloyd, O. E. Semonin, M. C. Beard, and A. J. Nozik, "Stability assessment on a 3% bilayer PbS/ZnO quantum dot heterojunction solar cell," *Advanced Materials*, vol. 22, no. 33, pp. 3704–3707, 2010.
- [3] J. J. Choi, Y. F. Lim, M. B. Santiago-Berrios et al., "PbSe Nanocrystal Excitonic Solar Cells," *Nano Letters*, vol. 9, no. 11, pp. 3749–3755, 2009.
- [4] T. Ju, R. L. Graham, G. Zhai et al., "High efficiency mesoporous titanium oxide PbS quantum dot solar cells at low temperature," *Applied Physics Letters*, vol. 97, no. 4, Article ID 043106, 2010.
- [5] J. M. Luther, M. Law, M. C. Beard et al., "Schottky solar cells based on colloidal nanocrystal films," *Nano Letters*, vol. 8, no. 10, pp. 3488–3492, 2008.
- [6] J. Tang, L. Brzozowski, D. A. R. Barkhouse et al., "Quantum dot photovoltaics in the extreme quantum confinement regime: the surface-chemical origins of exceptional air- and light-stability," *ACS Nano*, vol. 4, no. 2, pp. 869–878, 2010.
- [7] W. Ma, J. M. Luther, H. Zheng, Y. Wu, and A. P. Alivisatos, "Photovoltaic devices employing ternary PbS<sub>x</sub>Se<sub>1-x</sub> nanocrystals," *Nano Letters*, vol. 9, no. 4, pp. 1699–1703, 2009.
- [8] J. Van De Lagemaat, N. G. Park, and A. J. Frank, "Influence of electrical potential distribution, charge transport, and recombination on the photopotential and photocurrent conversion efficiency of dye-sensitized nanocrystalline TiO<sub>2</sub> solar cells: a study by electrical impedance and optical modulation techniques," *Journal of Physical Chemistry B*, vol. 104, no. 9, pp. 2044–2052, 2000.
- [9] N. Kopidakis, K. D. Benkstein, J. Van De Lagemaat, and A. J. Frank, "Transport-limited recombination of photocarriers in dye-sensitized nanocrystalline TiO<sub>2</sub> solar cells," *Journal of Physical Chemistry B*, vol. 107, no. 41, pp. 11307–11315, 2003.
- [10] B. Liu and E. S. Aydil, "Growth of oriented single-crystalline rutile TiO<sub>2</sub> nanorods on transparent conducting substrates for dye-sensitized solar cells," *Journal of the American Chemical Society*, vol. 131, no. 11, pp. 3985–3990, 2009.
- [11] K. Zhu, N. R. Neale, A. Miedaner, and A. J. Frank, "Enhanced charge-collection efficiencies and light scattering in dye-sensitized solar cells using oriented TiO<sub>2</sub> nanotubes arrays," *Nano Letters*, vol. 7, no. 1, pp. 69–74, 2007.
- [12] A. Guchgait, A. K. Rath, and A. J. Pal, "Near-IR activity of hybrid solar cells: enhancement of efficiency by dissociating excitons generated in PbS nanoparticles," *Applied Physics Letters*, vol. 9, no. 7, article 073505, 3 pages, 2010.
- [13] N. Barati, M. A. F. Sani, H. Ghasemi, Z. Sadeghian, and S. M. M. Mirhoseini, "Preparation of uniform TiO<sub>2</sub> nanostructure film on 316L stainless steel by sol-gel dip coating," *Applied Surface Science*, vol. 255, no. 20, pp. 8328–8333, 2009.
- [14] J. Joo, S. G. Kwon, T. Yu et al., "Large-scale synthesis of TiO<sub>2</sub> nanorods via nonhydrolytic sol-gel ester elimination reaction and their application to photocatalytic inactivation of *E. coli*," *Journal of Physical Chemistry B*, vol. 109, no. 32, pp. 15297–15302, 2005.
- [15] M. A. Hines and G. D. Scholes, "Colloidal PbS nanocrystals with size-tunable near-infrared emission: observation of post-synthesis self-narrowing of the particle size distribution," *Advanced Materials*, vol. 15, no. 21, pp. 1844–1849, 2003.
- [16] J. M. Luther, M. Law, Q. Song, C. L. Perkins, M. C. Beard, and A. J. Nozik, "Structural, optical, and electrical properties of self-assembled films of PbSe nanocrystals treated with 1,2-ethanedithiol," *ACS Nano*, vol. 2, no. 2, pp. 271–280, 2008.
- [17] B. Mukherjee, B. Viswanath, and N. Ravishankar, "Functional nanoporous structures by partial sintering of nanorod assemblies," *Journal of Physics D*, vol. 43, no. 45, Article ID 455301, 2010.
- [18] B. R. Hyun, Y. W. Zhong, A. C. Bartnik et al., "Electron injection from colloidal PbS quantum dots into titanium dioxide nanoparticles," *ACS Nano*, vol. 2, no. 11, pp. 2206–2212, 2008.
- [19] B. -R. Hyun, A. C. Bartnik, L. Sun, T. Hanrath, and F. W. Wise, "Control of electron transfer from lead-salt nanocrystals to TiO<sub>2</sub>," *Nano Letters*, vol. 11, no. 5, pp. 2126–2132, 2011.
- [20] I. Robel, V. Subramanian, M. Kuno, and P. V. Kamat, "Quantum dot solar cells. Harvesting light energy with CdSe nanocrystals molecularly linked to mesoscopic TiO<sub>2</sub> films," *Journal of the American Chemical Society*, vol. 128, no. 7, pp. 2385–2393, 2006.
- [21] W. A. Tisdale, K. J. Williams, B. A. Timp, D. J. Norris, E. S. Aydil, and X. Y. Zhu, "Hot-electron transfer from semiconductor nanocrystals," *Science*, vol. 328, no. 5985, pp. 1543–1547, 2010.

## Research Article

# Electrical Transport Properties of Multilayered Single-Walled Carbon Nanotube Films

**Yanli Zhao and Wenzhi Li**

*Department of Physics, Florida International University, Miami, FL 33199, USA*

Correspondence should be addressed to Wenzhi Li, wenzhi.li@fiu.edu

Received 3 December 2011; Accepted 17 January 2012

Academic Editor: Rajaram S. Mane

Copyright © 2012 Y. Zhao and W. Li. This is an open access article distributed under the Creative Commons Attribution License, which permits unrestricted use, distribution, and reproduction in any medium, provided the original work is properly cited.

An improved layer-by-layer vacuum filtration method was adopted for the fabrication of single-walled carbon nanotube (SWCNT) films aiming at a series of SWCNT films with controllable thickness and density. The electrical transport properties of the multilayered SWCNT films have been investigated. With the constant film density, the decrease of the layer number of the SWCNT film results in an increase of the temperature coefficient of resistance (TCR). SWCNT film with 95% metallic nanotubes has shown a lower TCR than that of the SWCNT films with a low percentage of metallic nanotubes. The effect of thermal annealing and subsequent acid ( $\text{HNO}_3$ ) treatment on the electrical properties of the SWCNT films has also been investigated.

## 1. Introduction

Even though single-tube devices based on single-walled carbon nanotubes (SWCNTs) have excellent properties [1–3], these devices are usually fabricated randomly since it is very difficult to find two identical SWCNTs through currently available technology. Currently, the available technologies for SWCNT synthesis usually produce a mixture of nanotubes with varying diameters [4–8]. An as-prepared SWCNT can be either metallic or semiconducting depending on its chirality. In general, one-third of the synthesized SWCNTs are metallic, while the other two-thirds are semiconducting [9]. Even though the separation of metallic SWCNTs from a mixture of both metallic and semiconducting SWCNTs has recently become possible [10], the repeatable fabrication of two identical SWCNT devices is further than a near future work. From the application aspect, SWCNT films which contain SWCNTs with all kinds of chiralities are very attractive, since they suppress the differences among individual nanotubes.

Low temperature measurements may give some insight into the transport mechanism of SWCNT films, which could lead to an optimal SWCNT film with designed electrical properties [11]. In addition to being a potential replacement for ITO as a conductive and transparent electrode material, SWCNT thin films have also attracted a lot of attention recently due to their large bolometric photoresponse and

high temperature coefficient of resistance (TCR) [12]. High TCR SWCNT films are highly desired for its potential application in infrared (IR) sensor. Vacuum filtration has been found as an effective approach for repeatable fabrication of single-walled carbon nanotube (SWCNT) films with a designed thickness and film density [1]. In this work, an improved layer-by-layer vacuum filtration method was adopted for the fabrication of SWCNT films aiming at a series of SWCNT films with controllable thickness and density. Decrease of the thickness of the SWCNT film with a constant film density will result in an increase of the TCR and a large resistance. The effect of thermal annealing and  $\text{HNO}_3$  treatment on the electrical properties of SWCNT film has also been discussed. Aiming to ultimately produce an optimal SWCNT film with a high TCR, our experiment provides insight into the design and selection of SWCNT films.

## 2. Experiments

In this research, we used commercially available HiPco purified SWCNTs and high purity (95%) metallic SWCNTs from <http://www.NanoIntegris.com>. The HiPco SWCNTs are mixture of metallic and semiconducting nanotubes. Since no preferential growth for metallic and semiconducting SWCNTs is found in the HiPco process, it is reasonable to believe

TABLE 1: The fabrication parameters, thickness, sheet resistance, and TCR at 300 K of the SWCNT thin films.

Sample name	Sample Description	Thickness (nm)	Sheet resistance at room environment ( $\Omega/\square$ )	TCR (at 300 K)
1	1 mL SWCNT suspension, 2 layers	45	45780	-0.146
2	2 mL SWCNT suspension, 1 layer	35	10750	-0.112
3	2 mL metallic SWCNT suspension, 1 layer	35	5693	-0.060
4	2 mL SWCNT suspension, 3 layers	105	3210	-0.088
2a	Sample 2 after annealing at 300°C, 12 hours	35	104500	-0.136
4a	Sample 4 after annealing at 300°C, 12 hours	105	24100	-0.101
2aN	Sample 2a after HNO <sub>3</sub> treatment	35	19780	-0.055
4aN	Sample 4a after HNO <sub>3</sub> treatment	105	1012	-0.0186

that about one-third of the mixed HiPco SWCNTs could be metallic nanotubes [9]. The NanoIntegris SWCNTs has 95% metallic SWCNTs which was extracted from mixed SWCNTs via an available process called density gradient centrifugation (DGC) as reported in [13]. When the samples were purchased, the NanoIntegris SWCNTs were already dispersed in aqueous solution with some water-soluble surfactants and the HiPco SWCNTs were in dry powder form. To make an aqueous solution of the HiPco SWCNTs, a surfactant (Triton-100) was used to help to disperse the nanotubes, followed by sonication process and a centrifugation process. The SWCNTs powder was dispersed in aqueous solutions of 1% v/v surfactant (Triton-100) via 1-hour ultrasonication and 0.5-hour centrifugation. The concentration of the obtained HiPco suspension is about  $5 \times 10^{-3}$  mg/mL. The well-dispersed NanoIntegris SWCNT suspension was diluted to the same concentration as that of the obtained HiPco SWCNT suspension, further sonication and centrifugation process were not needed for the NanoIntegris SWCNT suspension. To prepare a nanotube film, an improved layer-by-layer vacuum filtration method [14, 15] was adopted to make single- and multilayered SWCNT films. The dispersed HiPco and NanoIntegris SWCNT suspensions were vacuum-filtered onto 0.1  $\mu\text{m}$  pore size mixed cellulose ester membrane (Millipore) and followed by washing with copious quantities of deionized water to remove the surfactants (Triton-100 and other surfactants if any). To transfer the nanotube film to a glass substrate, the still wet membrane was placed onto the substrate with film side down, which makes the nanotube film intimately contact with the glass substrate. The assembly was subsequently covered with a piece of clean filter paper to absorb the moisture and compressed with a 2 kg mass to keep the thin film flat for overnight. Then, the dried membrane was simply peeled off from the membrane/nanotube/glass sample. The density of each layer of the multilayered SWCNT films can be controlled by the amount of SWCNT in the suspension, and the multilayered SWCNT films have been prepared by a layer-by-layer vacuum filtration method. The so-called layer-by-layer method is described as follows: after the first layer of SWCNTs has been transferred to the glass substrate, a second vacuum-filtrated layer of SWCNTs will be transferred on the first layer, and the third vacuum-filtrated layer will be transferred on the second layer, and so on. In the multilayered SWCNT film, the SWCNTs in the same

layer may be interwoven while the SWCNTs at the contact region of two adjacent layers will not interweave but a simple contact. In this experiment, to investigate the effect of the layer structure, density, and type of SWCNTs on the electrical properties of the SWCNT films, the following SWCNT film samples are prepared and tabulated in Table 1. Sample 1 has two layers, each layer was prepared using 1 mL HiPco SWCNT solution; sample 2 has only one layer prepared from 2 mL HiPco SWCNT solution; sample 3 has one layer prepared from 2 mL NanoIntegris metallic SWCNTs; sample 4 has three layers, each layer was prepared from 2 mL HiPco SWCNT solution. The as-prepared SWCNT films were thoroughly cleaned in acetone and then in ethanol for future electrical property measurements. Post treated samples (samples 2a–4aN) were prepared by annealing the as-prepared SWCNT films at 300°C in an Ar gas environment for 24 hours with and without subsequent HNO<sub>3</sub> treatments. The HNO<sub>3</sub> treatment was carried out by submerging the annealed nanotube/glass sample in 12 M HNO<sub>3</sub> for 0.5 hrs.

Atomic force microscopy (AFM) topography images of the SWCNT thin films were acquired in the tapping mode using a Multimode AFM (Veeco Instruments). AFM was also used to measure the thickness of the SWCNT films. During the measurement, the AFM tip scans across the lateral edge between SWCNT film and the bare glass substrate. The scan range is large enough (more than 50  $\mu\text{m}$ ) to avoid the inaccuracy originating from the difference between the SWCNT film's edge and its inner part. The vertical distance (height) between the step of SWCNT film and the bare glass substrate was determined. Several points have been measured by scanning from SWCNT film to glass substrate to get an average height with a scan rate of 0.5 Hz. The thickness of SWCNT films is defined as the average height obtained from the AFM measurements. The root-mean-square (RMS) roughness of the SWCNT film surface is typically less than 10 nm.

The strip electrodes on the SWCNT thin film were painted using commercially available Ag paste (Ted Pella Inc.), then silver wire was used to contact the Ag strip electrodes and the sample stage of a cryostat (VPF-500, Janis Research) for electrical property tests. To measure the contact resistance, the same-sized strip electrodes with different spacing between the adjacent ones were designed on the same SWCNT film. In this work, the width of the SWCNT films

was 5 mm, and the spacing between the adjacent electrodes varied from 2 mm to 8 mm. All electrical property tests were conducted using a Keithley 4200 SC semiconductor analyzer. The resistance between the electrodes with different spacing was then measured and used to determine the contact resistance of the silver/nanotube contact and the intrinsic resistance of the SWCNT films [1, 16]. For comparison, the electrical properties of some SWCNT films have also been measured with four-point method. Our measurements showed that the contact resistance was about 10 times smaller than the intrinsic resistance of the SWCNT film.

### 3. Results and Discussion

Table 1 tabulated the detailed information of all SWCNT films used in this experiments. Sample 1 is a two-layered SWCNT film which was prepared with a layer-by-layer process as mentioned in the experimental part. During the process, 1 mL SWCNT suspension was used for each layer of sample 1. Sample 2 is a single-layer SWCNT film which was prepared with 2 mL SWCNT suspension. The thickness of the obtained films is 45 nm for sample 1, and 35 nm for sample 2. Considering the same film dimension, the same total amount of SWCNTs used, and the different thickness for these two samples, it is easily to know that sample 1 has a lower density than that of sample 2. Comparison of sample 1 with sample 2 reveals that the decrease of the density of SWCNT film results in the increase of the sheet resistance in room environment from 10750  $\Omega/\square$ , even though the same amount of SWCNT suspension was used during the vacuum filtration for the two samples. Sample 3 is a single-layer SWCNT film prepared with 2 mL SWCNT suspension containing high metallic SWCNT content. If we ignore the diameter difference of metallic and semiconducting SWCNTs, it is reasonable to believe that samples 2 and 3 have the same thickness and density since we use the same volume of SWCNT suspension with the same concentration. In the error range of our experiment, it does show the same thickness of these two samples (35 nm) measured by AFM. The sheet resistance of sample 3 is nearly half of that of sample 2 due to the higher metallic SWCNT content (95%) in sample 3 than that (33.3%) in sample 2. Sample 4 is a 3-layered sandwich SWCNT film, in which every layer is exactly the same as that in sample 2. The thickness of sample 4 is 105 nm, which is 3 times as thick as that of sample 2. It is expected that the measured sheet resistance of sample 4 should be one-third of that of sample 2. However, we find that the resistance of sample 4 is slightly lower than the expected value, as shown in Table 1. It is well known that the conductivity of SWCNT film is determined by percolation theory [1]. A universal power law of the form  $\sigma \propto (p - p_c)^\alpha$  is used to determine the relation between the conductivity ( $\sigma$ ) and the concentration of conducting channels ( $p$ ) near the percolation threshold ( $p_c$ ). The critical exponent  $\alpha$ , which provides an index of the system dimensionality, is 1.3 and 1.94 in theory for ideal 2D and 3D systems. In our experiment, the SWCNT film system dimensionality changes from

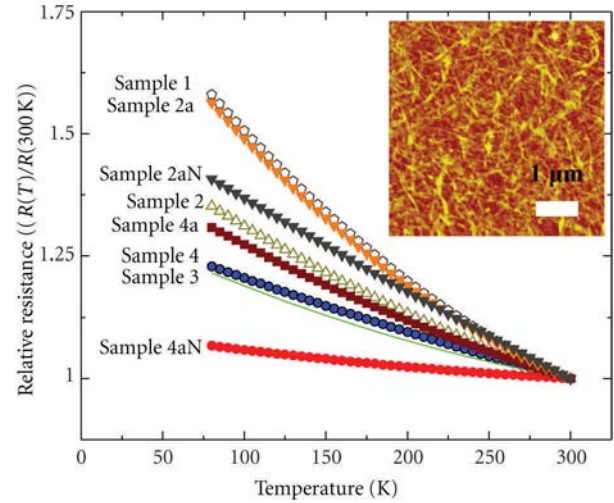


FIGURE 1: The change of relative resistance ( $R(T)/R(300\text{ K})$ ) with temperature for samples 1–4aN at temperature of 78–300 K. Inset shows an AFM image of a typical SWCNT film.

2D in sample 2 to 3D in sample 4, which may account for the smaller resistance value for sample 4 than the expected value.

Sample 2a is obtained by annealing sample 2 at 300°C in an Ar gas environment for 24 hours, comparison of sample 2a with sample 2 shows that the annealing treatment results in a rapid increase in the sheet resistance (from 10750  $\Omega/\square$  to 104500  $\Omega/\square$ ) at room temperature. The significant influence of annealing on the resistance of the SWCNT film was also observed in samples 4 and 4a, as shown in Table 1. The experimental results indicate clearly that the annealing will result in the increase of the resistance of SWCNT films. On the contrary, further  $\text{HNO}_3$  treatment leads to the obvious decrease of sheet resistance. As shown in Table 1, the sheet resistance of sample 2a was 104500  $\Omega/\square$ , but after further acid treatment the resistance was decreased to 19780  $\Omega/\square$  in sample 2aN. Similarly, the further acid treatment of sample 4a also resulted in a huge decrease of resistance from 24100  $\Omega/\square$  in sample 4a to 1012  $\Omega/\square$  in sample 4aN. The resistance decrease after acid treatment can be ascribed to the charge transfer [17–19] in the SWCNT films. The  $\text{HNO}_3$  oxidation will result in carboxyl ( $-\text{COOH}$ ) groups which will be attached to the defects sites and the SWCNT ends. The  $-\text{COOH}$  groups are electron acceptors and they will accept electrons transferred from SWCNTs. As a result, the density of holes in the p-type SWCNTs will increase and the separation between the Fermi level and the valence band will also decrease. Therefore, the electrical resistance of the SWCNT films after  $\text{HNO}_3$  treatment will decrease [17–19].

Figure 1 shows the change of relative resistance ( $R(T)/R(300\text{ K})$ ) with temperature for samples 1–4aN at the temperature range 80 K–300 K. The inset in Figure 1 shows a typical AFM image of the SWCNT films. A nanoscale porous network was formed due to the tubular structure of the carbon nanotubes. The root mean square (rms) roughness for the SWCNT film calculated from AFM data is about 7 nm, which is similar as the previous report [20]. The relative

resistance of all samples changes consecutively with temperature as well as SWCNT film density, thickness, and post treatments. The metallic SWCNT film (sample 3) does not demonstrate metallic properties in the measured temperature range, but as all of other samples, represents the negative  $\Delta R/\Delta T$ . As we know, the resistance of SWCNT film originates from two parts: one is from individual metallic SWCNTs and the other is from the junction resistance between metallic SWCNTs. It is believed that the junction resistance between metallic SWCNTs dominates the electrical transport, which may account for the negative ( $\Delta R/\Delta T$ ). Comparison of sample 1 with sample 2 reveals that the relative resistance decreases with film density. The decrease of film thickness leads to an increase in the relative resistance, as shown by the  $R(T)/R(300\text{ K})$  versus  $T$  plots for samples 2 and 4 in Figure 1. Figure 1 also shows the change of relative resistance of the SWCNT films before and after thermal anneal (plots for samples 2 and 2a, and plots for samples 4 and 4a) and after further  $\text{HNO}_3$  treatment (plots for 2aN and 4aN). It demonstrates that thermal anneal results in the increase of the relative resistance, while further  $\text{HNO}_3$  treatment will lead the decrease of the relative resistance.

Figure 2 depicts the variation in TCR for samples 1–4 as a function of temperature, which is deduced from Figure 1 with the formula  $\text{TCR} = (\Delta R/\Delta T)/R$ , where  $R$  is the relative resistance at temperature  $T$  and is shown in Figure 1. The absolute value of TCR changes with the density, thickness, and the metallic SWCNT content in SWCNT films, which originates from the different transport mechanism for these SWCNT films prepared under different parameters. By comparing the TCR versus  $T$  plots for samples 1 and 2, one can see that the magnitude of the TCR of higher density sample 2 is smaller than that of lower density sample 1. This result reveals that the increase of SWCNT film density results in a decrease in the TCR absolute value. From the TCR versus  $T$  plots of samples 2 and 3, it can be seen that magnitude of TCR decreases with the increase of the metallic SWCNT content in the SWCNT film. It is postulated that the positive TCR value for individual metallic SWCNT account for the low TCR magnitude of the SWCNT film with high metallic SWCNT content [21]. The TCR versus  $T$  curves for samples 2 and 4 shows the trend that the TCR absolute value for the same density of SWCNT film decreases with the thickness of the SWCNT film.

Figure 3 shows the typical TCR~ $T$  plots for samples 2 and 4 before and after annealing and acid treatments. Before and after the thermal annealing, the TCR absolute values increase from 0.112 (sample 2) to 0.136 (sample 2a) and from 0.088 (sample 4) to 0.101 (sample 4a) at 300 K. The TCR absolute value for the low density SWCNT film (sample 1) at 300 K is 0.146, which is the largest one among all samples, even larger than the annealed SWCNT film sample 2a, see Table 1. This result suggests that thermal annealing of sample 1 may result in even larger TCR values than that of all samples prepared here. Figure 3 shows that  $\text{HNO}_3$  treatment to the annealed samples will result in a remarkable decrease in the TCR absolute value, see the plots for samples 2aN and 4aN in Figure 3. As we know, the as-prepared SWCNT film

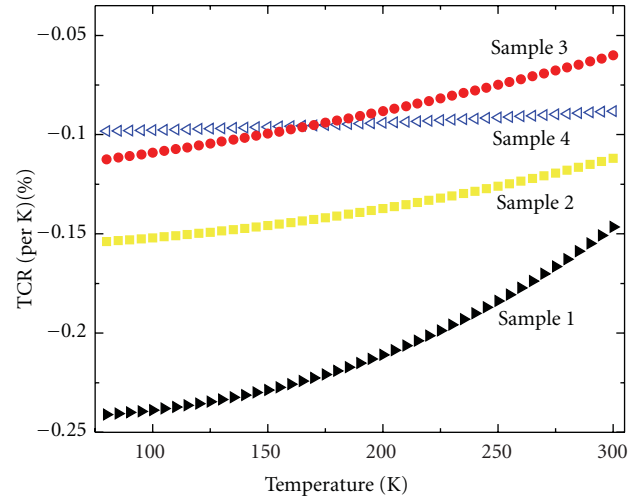


FIGURE 2: The variation of TCR for sample 1–4 as a function of temperature.

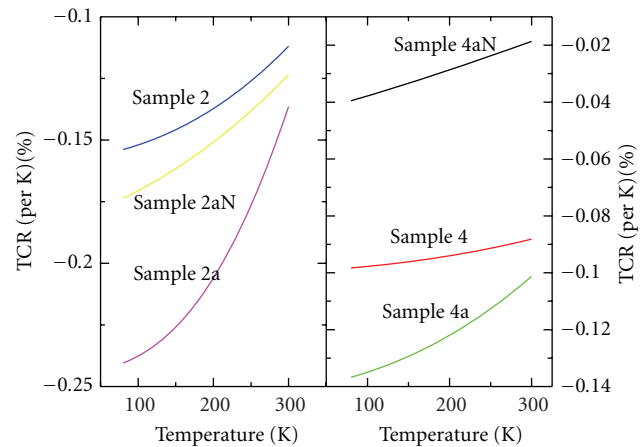


FIGURE 3: TCR~ $T$  plots for as-prepared, annealed, and acid-treated one- and three-layered SWCNT films.

is of p-type which may originate from the acid-reflux-based purification process and atmospheric impurities, such as oxygen gas. Thermal anneal can remove the p-type dopant and make the SWCNT more semiconducting, which may account for the increase of TCR after annealing. On the other hand, the decrease of the TCR of the acid-treated SWCNT film means that  $\text{HNO}_3$  treatment makes the annealed SWCNT film more metallic.

A careful investigation on the change of relative resistance and TCR with temperature before and after the  $\text{HNO}_3$  treatment for samples 2 and 4, as shown in Figures 1 and 3, demonstrates some differences of the electrical properties for the one- and three-layered samples. The relative resistance and TCR for sample 2aN are greater than those for the as-prepared sample 2 but smaller than those for the annealed sample 2a. However, the relative resistance and TCR for sample 4aN are smaller than those of the as-prepared sample 4 and the annealed sample 4a. The different changing trends of the relative resistance and TCR of acid-treated samples

2aN and 4aN may be the result of the aforementioned 2D to 3D system transition when the SWCNT film changes from one layer to three layers. The sheet resistance at room temperature for these samples as shown in Table 1 also indicates the possible 2D to 3D system transition. A more profound effect of HNO<sub>3</sub>-treatment on sample 4 than that on sample 2 is expected not only based on the transition of the SWCNT film dimensionality. Compared with sample 2, sample 4 has three layers, the SWCNTs in the same layer may be interwoven while the SWCNTs at the contact region of two adjacent layers will not interweave but have a simple contact. The intercalation of HNO<sub>3</sub> between the layers may also account for the obvious difference of relative resistance and TCR between samples 2 and 4 upon acid treatment [22, 23].

#### 4. Conclusions

In this work, the low temperature electrical transport properties of the multilayered single-walled carbon nanotube (SWCNT) films have been investigated experimentally. The temperature coefficient of resistance (TCR) of SWCNT films with layered structure, controllable thickness, density and volume ratio of metallic, and semiconducting SWCNTs has been studied. The decrease of SWCNT film density, decrease of metallic SWCNT content in SWCNT film, and the thermal annealing treatment are shown to be effective approaches to obtain a SWCNT film with a large TCR absolute value. Our experimental results may provide more hints on the application of SWCNT film in bolometers.

#### Acknowledgment

This work was supported by the National Science Foundation under Grant DMR-0548061.

#### References

- [1] L. Hu, D. S. Hecht, and G. Gruner, "Percolation in transparent and conducting carbon nanotube networks," *Nano Letters*, vol. 4, no. 12, pp. 2513–2517, 2004.
- [2] Z. Yao, C. L. Kane, and C. Dekker, "High-field electrical transport in single-wall carbon nanotubes," *Physical Review Letters*, vol. 84, no. 13, 2000.
- [3] A. Javey, H. Kim, M. Brink et al., "High- $\kappa$  dielectrics for advanced carbon-nanotube transistors and logic gates," *Nature Materials*, vol. 1, no. 4, pp. 241–246, 2002.
- [4] Z. Wu, Z. Chen, X. Du et al., "Transparent, conductive carbon nanotube films," *Science*, vol. 305, no. 5688, pp. 1273–1276, 2004.
- [5] C.-S. Woo, C.-H. Lim, C.-W. Cho et al., "Fabrication of flexible and transparent single-wall carbon nanotube gas sensors by vacuum filtration and poly(dimethyl siloxane) mold transfer," *Microelectronic Engineering*, vol. 84, no. 5-8, pp. 1610–1613, 2007.
- [6] C. Lim, D.-H. Min, and S.-B. Lee, "Direct patterning of carbon nanotube network devices by selective vacuum filtration," *Applied Physics Letters*, vol. 91, no. 24, 2007.
- [7] K. Lee, Z. Wu, Z. Chen, F. Ren, S. J. Pearton, and A. G. Rinzler, "Single wall carbon nanotubes for p-type ohmic contacts to GaN light-emitting diodes," *Nano Letters*, vol. 4, no. 5, pp. 911–914, 2004.
- [8] M. W. Rowell, M. A. Topinka, M. D. McGehee et al., "Organic solar cells with carbon nanotube network electrodes," *Applied Physics Letters*, vol. 88, no. 23, Article ID 233506, 2006.
- [9] M. S. Dresselhaus, G. Dresselhaus, R. Saito, and A. Jorio, "Raman spectroscopy of carbon nanotubes," *Physics Reports*, vol. 409, no. 2, pp. 47–99, 2005.
- [10] A. A. Green and M. C. Hersam, "Colored semitransparent conductive coatings consisting of monodisperse metallic single-walled carbon nanotubes," *Nano Letters*, vol. 8, no. 5, pp. 1417–1422, 2008.
- [11] Z. Li, H. R. Kandel, E. Dervishi et al., "Does the wall number of carbon nanotubes matter as conductive transparent material?" *Applied Physics Letters*, vol. 91, no. 5, Article ID 053115, 2007.
- [12] R. Lu, G. Xu, and J. Z. Wu, "Effects of thermal annealing on noise property and temperature coefficient of resistance of single-walled carbon nanotube films," *Applied Physics Letters*, vol. 93, no. 21, 2008.
- [13] A. A. Green and M. C. Hersam, "Colored semitransparent conductive coatings consisting of monodisperse metallic single-walled carbon nanotubes," *Nano Letters*, vol. 8, no. 5, pp. 1417–1422, 2008.
- [14] Z. Wu, Z. Chen, X. Du et al., "Transparent, conductive carbon nanotube films," *Science*, vol. 305, no. 5688, pp. 1273–1276, 2004.
- [15] Y. L. Zhao and W. Z. Li, "Effect of annealing and HNO<sub>3</sub>-treatment on the electrical properties of transparent conducting carbon nanotube films," *Microelectronic Engineering*, vol. 87, no. 4, pp. 576–579, 2010.
- [16] F. M. Blighe, Y. R. Hernandez, W. J. Blau, and J. N. Coleman, "Observation of percolation-like scaling—far from the percolation threshold—in high volume fraction, high conductivity polymer-nanotube composite films," *Advanced Materials*, vol. 19, no. 24, pp. 4443–4447, 2007.
- [17] M. Penza, G. Cassano, R. Rossi et al., "Effect of growth catalysts on gas sensitivity in carbon nanotube film based chemiresistive sensors," *Applied Physics Letters*, vol. 90, no. 10, Article ID 103101, 2007.
- [18] A. Hirsch, "Functionalization of single-walled carbon nanotubes," *Angewandte Chemie*, vol. 41, no. 11, pp. 1853–1859, 2002.
- [19] E. B. Barros, A. G. S. Filho, V. Lemos et al., "Charge transfer effects in acid treated single-wall carbon nanotubes," *Carbon*, vol. 43, no. 12, pp. 2495–2500, 2005.
- [20] Y. Zhou, L. Hu, and G. Grüner, "A method of printing carbon nanotube thin films," *Applied Physics Letters*, vol. 88, no. 12, 2006.
- [21] E. Pop, D. A. Mann, K. E. Goodson, and H. Dai, "Electrical and thermal transport in metallic single-wall carbon nanotubes on insulating substrates," *Journal of Applied Physics*, vol. 101, no. 9, Article ID 093710, 2007.
- [22] G. U. Sumanasekera, J. L. Allen, S. L. Fang, A. L. Loper, A. M. Rao, and P. C. Eklund, "Electrochemical oxidation of single wall carbon nanotube bundles in sulfuric acid," *Journal of Physical Chemistry B*, vol. 103, no. 21, pp. 4292–4297, 1999.
- [23] Y. Wang, C. A. Di, Y. Liu et al., "Optimizing single-walled carbon nanotube films for applications in electroluminescent devices," *Advanced Materials*, vol. 20, no. 23, pp. 4442–4449, 2008.